Article:
Capel Berdiell, I orcid.org/0000-0003-3828-7097, Kulmaczewski, R orcid.org/0000-0002-3855-4530 and Halcrow, MA orcid.org/0000-0001-7491-9034 (2017) Iron(II) Complexes of 2,4-Dipyrazolyl-1,3,5-triazine Derivatives - The Influence of Ligand Geometry on Metal Ion Spin State. Inorganic Chemistry, 56 (15). pp. 8817-8828. ISSN 0020-1669

https://doi.org/10.1021/acs.inorgchem.7b00699

Iron(II) Complexes of 2,4-Dipyrazolyl-1,3,5-Triazine Derivatives – the Influence of Ligand Geometry on Metal Ion Spin State

*Izar Capel Berdiell, Rafal Kulmaczewski and Malcolm A. Halcrow**

School of Chemistry, University of Leeds, Woodhouse Lane, Leeds LS2 9JT, UK.

ABSTRACT

Seven [FeL_2][BF_4]$_2$ complex salts have been prepared, where L is a 6-substituted 2,4-di(pyrazol-1-yl)-1,3,5-triazine (bpt) derivative. The complexes are all crystallographically high-spin, and exhibit significant distortions from an ideal D_{2d}-symmetric coordination geometry. In one case, an unusual type of metal ion disorder was observed among a cubic array of ligands in the crystal lattice. The complexes are also high-spin between 3-300 K in the solid state and, where measured, between 239-333 K in CD_3CN solution. This result is unexpected, since homoleptic iron(II) complexes of related 2,6-di(pyrazol-1-yl)pyridine, 2,6-di(pyrazol-1-yl)pyrazine and 2,6-di(pyrazol-1-yl)pyrimidine derivatives often exhibit thermal spin-crossover behavior. Gas phase DFT calculations confirm the high-spin form of $[Fe(bpt)_2]^{2+}$ and its derivatives is stabilized relative to iron(II) complexes of the other ligand types. This reflects a weaker Fe/pyrazolyl σ-bonding interaction, which we attribute to a small narrowing of the chelate ligand bite angle associated with the geometry of the 1,3,5-triazinyl ring. Hence, the high-spin state of $[Fe(bpt)_2]^{2+}$ centers does not reflect the electronic properties of its heterocyclic ligand donors, but is imposed by the bpt ligand conformation. A high-spin homoleptic iron(III) complex of one of the bpt derivatives was also synthesized.

Introduction

Spin-crossover (SCO) complexes are an important class of molecular switch for molecular materials and nanoscience research.[1-3] An SCO transition involves a change in spin state at metal ion centers in a material, causing changes to a number of its physical properties including its colour, paramagnetism[4] and conductivity.[5] The associated expansion or contraction of the metal ion coordination sphere can also be coupled to guest uptake or release in a porous solid,[6] or a mechanical response in an actuating device.[7] SCO compounds have also been used to form nanoparticles or thin films that retain their SCO properties at length scales of 10^1 nm and above,[8] while modulation of a single molecule junction by a field-induced spin transition has also been conclusively demonstrated.[9] The production of new molecules and materials with pre-defined spin state properties for these applications is an important problem of coordination chemistry and crystal engineering.[10]

An important family of compounds in SCO research are derivatives of $[Fe(bpp)_2]^{2+}$, where bpp is 2,6-di(pyrazol-1-yl)pyridine (Chart 1).[11,12] The ligand field in $[Fe(bpp)_2]^{2+}$ centres is appropriate for SCO near room temperature, and can be tuned in a predictable way by ligand substituents (R^1 or R^2, Chart 1).[13] Moreover, derivatizing the bpp framework introduces secondary functionality to $[Fe(bpp)_2]^{2+}$ complexes, including surface tether groups;[14] redox active,[15] magnetically active[16] or emissive centers;[17] photoisomerizable groups;[18] and, additional metal-binding domains to give ditopic bpp derivatives.[19] While this is a powerful method to produce multifunctional SCO compounds, multi-step syntheses are often required to produce the appropriate bpp ligands. We are therefore seeking alternative ligand classes offering more accessible routes to multifunctional SCO materials.

Chart 1 The ligand types discussed in this work, and their common substitution patterns.

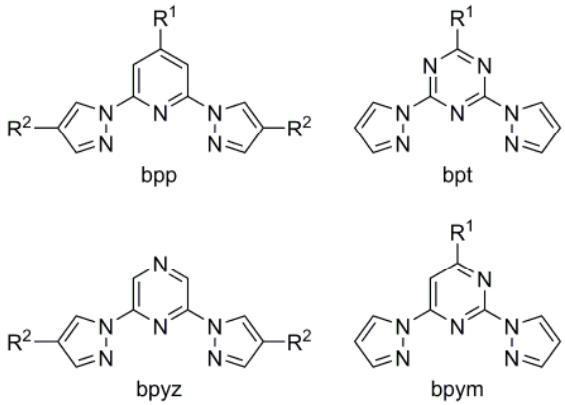

As well as bpp, the related ligand types 2,6-di(pyrazol-1-yl)pyrazine (bpyz)[20,21] and 2,6-di(pyrazol-1-yl)pyrimidine (bpym, Chart 1)[22] are known to afford SCO-active iron(II) complexes. Hence, we decided to investigate iron complexes of ligands derived from 2,4-di(pyrazol-1-yl)-1,3,5-triazine (bpt). The parent bpt ligand (R^1 = H, Chart 1) has not been described before. However, bpt derivatives substituted at the triazinyl *C*6 position ($R^1 \neq$ H) are well known ligands for *d*- and *f*-block metals,[23] with derivatives bearing dialkylamino R^1 substituents (Chart 1) being effective sensitizers for lanthanide emission.[24] Other studies of bpt coordination chemistry have focused on fluxionality of coordinated ligands,[25] or on polymetallic complexes[26] and coordination polymers[27] supported by bpt co-ligands. However, few homoleptic $[M(bpt)_2]^{n+}$ (M^{n+} = a transition ion) complexes have been reported up to now,[28] and iron(II) complexes of this type remain to be explored. The unusual crystal engineering properties afforded by the π-acid 1,3,5-triazinyl ring is another attractive feature of the $[M(bpt)_2]^{n+}$ system,[23,28,29] while SCO complexes of other ligand types incorporating coordinated[30,31] or uncoordinated[32] 1,3,5-triazinyl moieties are also well known.

We report here the iron complex chemistry of seven ligands of the bpt type. Since the inductive properties of R^1 ligand substituents strongly influence the spin state of $[Fe(bpp)_2]^{2+}$ derivatives (Chart 1),[13] bpt ligands bearing a range of different heteroatom R^1 substituents have been investigated (Chart 2). DFT calculations are also included, to rationalize the unexpected spin state properties of mononuclear $[Fe(bpt)_2]^{2+}$ centers. These provide new insight into the subtleties of ligand design for control of metal ion spin states in spin-crossover, and in other areas of chemistry.[10]

Chart 2 The bpt derivatives used in this work.

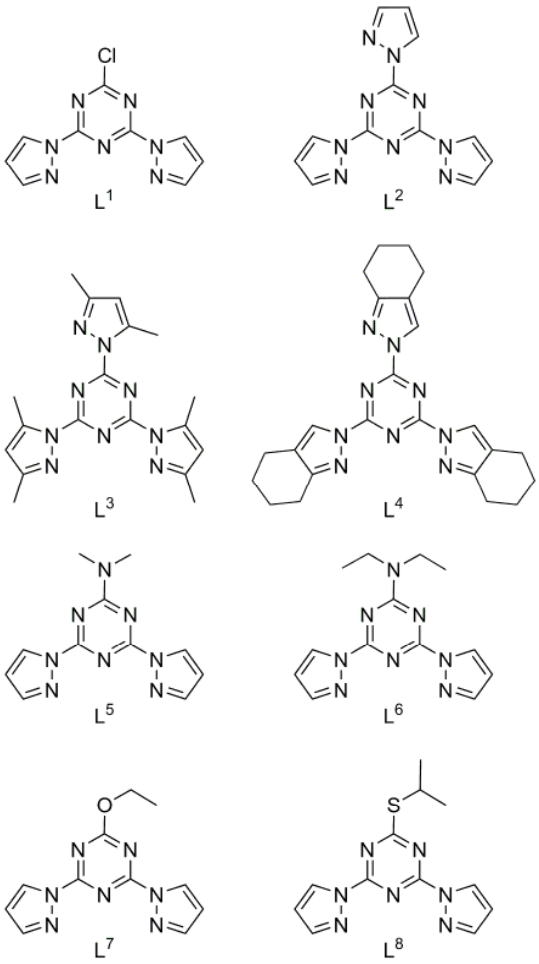

Experimental

Unless otherwise stated, all reactions were carried out in air using AR-grade solvents. 2,4,6-Tri(pyrazol-1-yl)-1,3,5-triazine (L^2),[28,33] 2,4,6-tri(3,5-dimethylpyrazol-1-yl)-1,3,5-triazine (L^3)[28] and 2,4-di(pyrazol-1-yl)-6-(diethylamino)-1,3,5-triazine (L^6)[28] were prepared by the literature procedures. Chromatographic separations employed Merck Geduran Si 60 silica gel.

Synthesis of 2,4-di(pyrazol-1-yl)-6-chloro-1,3,5-triazine (L^1). Cyanuric chloride (1.35 g, 7.3 mmol) was added in small portions to a stirred solution of pyrazole (1.0 g, 14.7 mmol) in THF (125 cm^3) at room temperature. The resultant pale yellow suspension was stirred for 6 hr. The solvent was removed *in vacuo*, water (100 cm^3) was added to the residue, and the aqueous mixture was extracted with dichloromethane (300 cm^3). The dried extracts were evaporated to dryness to give a blue/white solid. The white product was purified by elution over silica gel (eluent: EtOAc, Rf: 0.58). Yield 0.61 g, 34%. Mp 168-170 ^{0}C (lit 161–163 ^{0}C[34]). Elemental analysis for $C_9H_6ClN_7$ found, (calcd) (%) C 43.4 (43.7), H 2.80 (2.44), N 39.2 (39.6). ESMS *m/z* 248.0 ($[HL^1]^+$), 270.0 ($[NaL^1]^+$), 517.1 ($[Na(L^1)_2]^+$). ^{1}H NMR ($CDCl_3$) δ 6.61 (dd, 1.5 and 2.9 Hz, 2H, Pz H^4), 7.96 (d, 1.5 Hz, 2H, Pz H^3), 8.68 (d, 2.9 Hz, 2H, Pz H^5). ^{13}C NMR ($CDCl_3$) δ 110.9 (2C, Pz C^4), 130.7 (2C, Pz C^5), 146.6 (2C, Pz C^3), 162.9 (2C, Trz $C^{2/4}$), 173.6 (1C, Trz C^6).

Synthesis of 2,4,6-tri(4,5,6,7-tetrahydroindazol-2-yl)-1,3,5-triazine (L^4). Solid 4,5,6,7 tetrahydroindazole (2.07 g, 16.2 mmol) was added to a stirred suspension of NaH (60 wt % in mineral oil; 0.33 g, 8.1 mmol) in THF (125 cm^3) under an N_2 atmosphere, while keeping the temperature below 0 °C. After H_2 evolution had ceased, cyanuric chloride (1.0 g, 5.4 mmol) was carefully added while maintaining the low temperature. The pale yellow suspension was then

stirred for 4 hr. The solvent was removed *in vacuo,* and water (100 cm^3) was carefully added to the residue. The aqueous mixture was extracted with dichloromethane (300 cm^3) and chloroform (100 cm^3), and the combined organic layer was dried with $MgSO_4$ then evaporated to dryness. Pure L^4 was isolated following elution through silica gel (eluent: ethyl acetate→acetone gradient, Rf: 0.08→0.34) as a white powder. Yield 0.54 g, 23 %. Mp 345 ^{0}C dec. Elemental analysis for $C_{24}H_{27}N_9$ found, (calcd) (%) C 64.7 (65.3), H 6.30 (6.16), N 28.1 (28.5). ESMS *m/z* 442.3 ($[HL^4]^+$), 905.5 ($[Na(L^4)_2]^+$). ^{1}H NMR ($CDCl_3$) δ 1.78 (m, 6H, H_4Ind H^6), 1.84 (m, 6H, H_4Ind H^5), 2.62 (t, 6.0 Hz, 6H, H_4Ind H^7), 2.82 (t, 6.0 Hz, 6H, H_4Ind H^4), 8.42 (s, 3H, H_4Ind H^3). ^{13}C NMR ($CDCl_3$) δ 20.5 (3C, H_4Ind C^4), 22.9 (6C, H_4Ind C^5 + C^6), 24.0 (3C, H_4Ind C^7), 121.1 (3C, H_4Ind C^{3a}), 126.9 (3C, H_4Ind C^3), 157.0 (3C, H_4Ind C^{7a}), 162.9 (3C, Trz $C^{2/4/6}$).

Synthesis of 2,4-di(pyrazol-1-yl)-6-(dimethylamino)-1,3,5-triazine (L^5). A mixture of L^2 (1.5 g, 5.3 mmol) and dimethylamine (40 % aqueous solution; 1.1 cm^3, 8.4 mmol) in chloroform (15 cm^3) was stirred at 298 K for 1.5 hrs. Water (25 cm^3) was added and the mixture stirred for a further 10 min. The organic phase was dried over $MgSO_4$ and evaporated to dryness. The white compound was isolated *via* silica gel chromatography (eluent: ethyl acetate→acetone gradient, Rf: 0.23→0.33). Yield 0.88 g, 65 %. Mp 209-211 ^{0}C. Elemental analysis for $C_{11}H_{12}N_8$ found, (calcd) (%) C 51.7 (51.6), H 4.77 (4.72), N 43.9 (43.7). ESMS *m/z* 257.1 ($[HL^5]^+$), 279.1 ($[NaL^5]^+$), 535.2 ($[Na(L^5)_2]^+$). ^{1}H NMR ($CDCl_3$) δ 3.30 (s, 6H, N{CH_3}$_2$), 6.42 (dd, 1.6 and 2.5 Hz, 2H, Pz H^4), 7.80 (br s, 2H, Pz H^3), 8.60 (d, 2.5 Hz, 2H, Pz H^5). ^{13}C NMR ($CDCl_3$) δ 36.8 (2C, N{*C*H$_3$}$_2$), 108.6 (2C, Pz C^4), 129.8 (2C, Pz C^5), 144.3 (2C, Pz C^3), 162.0 (2C, Trz $C^{2/4}$), 166.0 (1C, Trz C^6).

Synthesis of 2,4-di(pyrazol-1-yl)-6-(isopropylsulfanyl)-1,3,5-triazine (L^8). A mixture of L^2 (0.80 g, 2.9 mmol) and sodium 2-propanethiolate (0.28 g, 2.85 mmol) in dichloromethane (10 cm^3) was stirred at room temperature for 3 hrs. Water (25 cm^3) was then added to the mixture and the organic phase was separated, dried over $MgSO_4$, and evaporated to a white residue. The pure compound was isolated as a white solid *via* silica gel chromatography (eluent: ethyl acetate, Rf: 0.65). Yield 0.23 g, 28 %. Mp 145-147 ^{0}C. Elemental analysis for $C_{12}H_{13}N_7S$: found, (calcd) (%) C 50.1 (50.2), H 4.64 (4.56), N 34.0 (34.1). ESMS *m/z* 288.1 ($[HL^8]^+$), 310.1 ($[NaL^8]^+$). ^{1}H NMR ($CDCl_3$) δ 1.53 (d, 6.8 Hz, 6H, SCH{CH_3}$_2$), 4.16 (heptet, 6.8 Hz, 1H, SCH{CH_3}$_2$), 6.56 (dd, 1.5 and 2.7 Hz, 2H, Pz H^4), 7.92 (br s, 2H, Pz H^3), 8.67 (d, 2.7 Hz, 2H, Pz H^5). ^{13}C NMR ($CDCl_3$) δ 22.6 (2C, SCH{CH$_3$}$_2$), 36.5 (1C, SCH{CH_3}$_2$), 109.9 (2C, Pz C^4), 130.3 (2C, Pz C^5), 145.5 (2C, Pz C^3), 161.1 (2C, Trz $C^{2/4}$), 186.2 (1C, Trz C^6).

Synthesis of $[Fe(L^2)_2][BF_4]_2$. Solid $Fe[BF_4]_2{\cdot}6H_2O$ (0.060 g, 0.17 mmol) was added to a stirred solution of L^2 (0.10 g, 0.36 mmol) in nitromethane (15 cm^3). The mixture was stirred, with warming if necessary, until all the solid had dissolved. The solution was concentrated to one-third its original volume and diethyl ether was added to afford a yellow precipitate, which was collected by filtration. The product was recrystallized by slow diffusion of diethyl ether vapor into a nitromethane solution of the complex. Yield 0.12 g, 85 %. Elemental analysis for $C_{24}H_{18}B_2F_8FeN_{18}$ found (calcd) (%) C, 36.6 (36.6), H, 2.34 (2.30), N, 31.8 (32.0). ESMS *m/z* 280.1 (67, $[HL^2]^+$), 302.1 (81, $[NaL^2]^+$), 307.1 (100, $[Fe(L^2)_2]^{2+}$), 329.5 (40, $[Fe(L^2)_2(O_2CH)]^{2+}$), 338.5 (41, $[Fe(L^2)_2(O_2CH)(OH_2)]^{2+}$), 438.6 (40, $[Fe_2Na(L^5)_2(OH_2)(NCMe)F_2(BF_4)]^{2+}$), 513.1 (5, [FeH(2,4-di{pyrazolyl}-6-oxo-1,3,5-triazinate)$_2$]$^+$), 563.1 (14, [Fe(L^2)(2,4-di{pyrazolyl}-6-oxo-1,3,5-triazinate)]$^+$), 581.2 (46, $[Na(L^2)_2]^+$), 633.1 (6, $[Fe(L^2)_2F]^+$). ^{1}H NMR (CD_3NO_2) δ 5.2 (2H,

uncoordinated Pz H^4), 6.1 (2H, uncoordinated Pz H^3), 8.4 (2H, uncoordinated Pz H^5), 43.8 (8H, coordinated Pz H^3 + H^5), 72.1 (4H, coordinated Pz H^4).

Synthesis of $[Fe(L^2)_2][ClO_4]_2$. Method as for $[Fe(L^2)_2][BF_4]_2$, using $Fe[ClO_4]_2{\cdot}6H_2O$ (0.062 g, 0.17 mmol). Yield 0.098 g, 71 %. Elemental analysis for $C_{24}H_{18}Cl_2FeN_{18}O_8$ found (calcd) (%) C, 35.3 (35.4), H, 2.23 (2.23) N, 30.9 (31.0).

Synthesis of $[Fe(L^7)_2][BF_4]_2$. Separate solutions of $Fe[BF_4]_2{\cdot}6H_2O$ (0.058 g, 0.17 mmol) and L^1 (0.10 g, 0.40 mmol) in ethanol (25 cm^3) were mixed at 60 °C, causing an immediate bright yellow coloration. The cooled solution was stored overnight at –15 °C to afford a yellow polycrystalline material, which was identified as $[Fe(L^7)_2][BF_4]_2$ by a crystal structure analysis. Yield 0.087 g, 69 %. Elemental analysis for $C_{22}H_{22}B_2F_8FeN_{14}O_2$ found (calcd) (%) C, 35.4 (35.5), H, 2.90 (2.98), N, 26.2 (26.3). ESMS *m*/*z* 195.5 (14, $[Na_2H(L^7)BF_4]^{2+}$), 258.1 (64, $[HL^7]^+$), 280.1 (44, $[NaL^7]^+$), 285.1 (100, $[Fe(L^7)_2]^{2+}$), 332.0 (6, $[Fe(L^7)F]^+$), 405.6 (18, $[Fe_3(L^7)_2(O_2CH)_2F_2]^{2+}$ or $[Fe_2Na(L^7)_2(OH_2)_2F_2BF_4]^{2+}$), 413.1 (7, $[Fe_2Na(L^7)_2(O_2CH)_2BF_4]^{2+}$), 537.2 (70, $[Na(L^7)_2]^+$), 589.1 (42, $[Fe(L^7)_2F]^+$), 605.1 (12, $[Na_2(L^7)_2(O_2CH)]^+$), 615.1 (14, $[Fe(L^7)_2(O_2CH)]^+$), 798.2 (4, $[Fe_2Na(L^7)_5(O_2CH)_2BF_4]^{2+}$). ^{1}H NMR ($CD_3CN$) δ –1.8 (6H, OCH_2CH_3), 4.1 (4H, OCH_2CH_3), 42.3 and 42.7 (both 4H, Pz H^3 + H^5), 70.0 (4H, Pz H^4).

Synthesis of the other complexes in this work. The same method, as described for $[Fe(L^3)_2][BF_4]_2$, was used for the rest of the complexes in this work. Filtered solutions of $Fe[BF_4]_2{\cdot}6H_2O$ (0.060 g, 0.17 mmol) in acetonitrile (30 cm^3), and of L^3 (0.12 g, 0.34 mmol) in dichloromethane (30 cm^3), were mixed at room temperature. After stirring for 30 mins, diethyl ether vapor was diffused directly into the reaction mixture to yield single crystals. The same

procedure, with the relevant ligand and either $Fe[BF_4]_2 \cdot 6H_2O$ or $Fe[ClO_4]_3 \cdot nH_2O$, as appropriate, afforded all the following compounds in (poly)crystalline form. Yields ranged from 61-82 %.

For $[Fe(L^3)_2][BF_4]_2$: orange crystals. Elemental analysis for $C_{36}H_{42}B_2F_8FeN_{18}$ found (calcd) (%) C, 45.1 (45.2), H, 4.32 (4.43), N, 26.3 (26.4). ESMS *m*/*z* 286.1 (6, [H(2,4-di{3,5-dimethyl pyrazolyl}-6-hydroxy-1,3,5-triazine)]$^+$), 364.1 (10, $[HL^3]^+$), 386.1 (13, $[NaL^3]^+$), 391.2 (100, $[Fe(L^3)_2]^{2+}$), 625.2 (4, [FeH(2,4-di{3,5-dimethylpyrazolyl}-6-oxo-1,3,5-triazinate)$_2$]$^+$), 703.1 (98, [Fe(L^3)(2,4-di{3,5-dimethylpyrazolyl}-6-oxo-1,3,5-triazinate)]$^+$), 749.1 (4, $[Na(L^3)_2]^+$), 801.3 (3, $[Fe(L^3)_2F]^+$). ^{1}H NMR (CD_3NO_2) δ 3.0 and 3.7 (both 6H, s, 2x uncoordinated Pz 3-CH_3 & 5-CH^3), 4.7 (s, 2H uncoordinated Pz H^4), 7.3 (s, 12H, coordinated Pz 5-CH_3), 18.3 (12H, coordinated Pz 3-CH_3), 76.7 (4H, coordinated Pz H^4). Weaker peaks were also observed at δ 21.7, 22.1, 64.3, 67.9, 70.3 and/or 88.2, with the latter four comprising up to 30 % of the sample.

For $[Fe(L^4)_2][BF_4]_2 \cdot CH_2Cl_2$: yellow crystals. Elemental analysis for $C_{48}H_{54}B_2F_8FeN_{18} \cdot CH_2Cl_2$ found (calcd) (%) C, 49.3 (49.1), H, 4.50 (4.71), N, 21.0 (21.0). ESMS *m*/*z* 442.1 (33, $[HL^4]^+$), 464.2 (16, $[NaL^4]^+$), 469.2 (100, $[Fe(L^4)_2]^{2+}$), 905.5 (3, $[Na(L^4)_2]^+$). ^{1}H NMR (CD_3CN) δ 1.4 and 1.5 (both 4H, uncoordinated H_4Ind H^5 + H^6), 3.0 and 4.0 (both 8H, coordinated H_4Ind H^5 + H^6), 5.0 and 5.8 (both 4H, uncoordinated H_4Ind H^4 + H^7), 8.0 (2H, uncoordinated H_4Ind H^3), 10.3 (8H, coordinated H_4Ind H^6), 12.8 (8H, coordinated H_4Ind H^7), 37.3 (4H, coordinated H_4Ind H^3).

For $[Fe(L^5)_2][BF_4]_2$: yellow crystals. Elemental analysis for $C_{22}H_{24}B_2F_8FeN_{16}$ found (calcd) (%) C, 35.7 (35.6), H, 3.17 (3.26), N, 30.1 (30.2). ESMS *m*/*z* 257.1 (100, $[HL^5]^+$), 279.1 (98, $[NaL^5]^+$), 284.1 (99, $[Fe(L^5)_2]^{2+}$), 404.2 (47, $[Fe_3(L^5)_2(O_2CH)_2F_2]^{2+}$ or $[Fe_2Na(L^5)_2(OH_2)_2F_2(BF_4)]^{2+}$), 535.2 (100, $[Na(L^5)_2]^+$), 587.1 (13, $[Fe(L^5)_2F]^+$), 655.2 (4, $[Fe(L^5)_2BF_4]^+$). ^{1}H NMR (CD_3CN) δ 16.0 (12H, N{CH_3}$_2$), 49.4 (8H, Pz H^3 + H^5), 72.6 (4H, Pz H^4).

For $[Fe(L^6)_2][BF_4]_2$: yellow crystals. Elemental analysis for $C_{26}H_{32}B_2F_8FeN_{16}$ found (calcd) (%) C, 38.9 (39.1), H, 3.90 (4.04), N, 27.9 (28.1). ESMS *m/z* 285.1 (9, $[HL^7]^+$), 307.1 (64, $[NaL^7]^+$), 312.1 (100, $[Fe(L^6)_2]^{2+}$), 591.3 (3, $[Na(L^6)_2]^+$). ^{1}H NMR (CD_3CN) δ 0.2 (12H, N{CH_2CH_3}$_2$), 10.6 (8H, N{CH_2CH_3}$_2$), 49.1 (8H, Pz H^3 + H^5), 72.0 (4H, Pz H^4).

For $[Fe(L^6)_2][ClO_4]_3$: black polycrystalline material. Elemental analysis for $C_{26}H_{32}Cl_3FeN_{16}O_{12}$ found (calcd) (%) C, 33.9 (33.8), H, 3.46 (3.50), N, 24.1 (24.3). ESMS *m/z* 312.1 (100, $[Fe(L^6)_2]^{2+}$).

For $[Fe(L^8)_2][BF_4]_2$: yellow crystals. Elemental analysis for $C_{24}H_{26}B_2F_8FeN_{14}S_2$ found (calcd) (%) C, 35.9 (35.8), H, 3.36 (3.26), N, 24.3 (24.4). ESMS *m/z* 246.1 (16, [H(2,4-di{pyrazolyl}-1,3,5-triazine-6-thiol)]$^+$), 268.1 (13, [Na(2,4-di{pyrazolyl}-1,3,5-triazine-6-thiol)]$^+$), 273.1 (66, [Fe(2,4-di{pyrazolyl}-1,3,5-triazine-6-thiol)$_2$]$^{2+}$), 288.1 (43, $[HL^8]^+$), 294.6 (67, [Fe(L^8)(2,4-di{pyrazolyl}-1,3,5-triazine-6-thiol)]$^{2+}$), 310.1 (98, $[NaL^8]^+$), 315.1 (100, $[Fe(L^8)_2]^{2+}$), 450.6 (51, $[Fe_2Na(L^8)_2F(BF_4)_2]^{2+}$), 545.1 (4, [FeH(2,4-di{pyrazolyl}-1,3,5-triazine-6-thiolate)$_2$]$^+$), 588.1 (7, [Fe(L^8)(2,4-di{pyrazolyl}-1,3,5-triazine-6-thiolate)]$^+$), 597.2 (63, $[Na(L^8)_2]^+$), 649.1 (32, $[Fe(L^8)_2F]^+$). ^{1}H NMR (CD_3NO_2) δ 1.0 (12H, SCH{CH_3}$_2$), 5.5 (2H, SC*H*{CH_3}$_2$), 44.3 (8H, Pz H^3 + H^5), 72.0 (4H, Pz H^4).

CAUTION! Although we have experienced no problems in handling the perchlorate salts in this study, metal-organic perchlorates are potentially explosive and should be handled with due care in small quantities.

Single crystal X-ray structure determinations

The diffraction data for α-$[Fe(L^2)_2][BF_4]_2$ were recorded at station I19 of the Diamond synchrotron (λ= 0.6998 Å). All the other crystallographic data were measured with an Agilent

Supernova dual-source diffractometer, using monochromated Cu-K_α (λ = 1.5418 Å) radiation. The diffractometer was fitted with Oxford Cryostream low-temperature devices. Experimental data (Tables S1 and S2) and refinement procedures for all the structure determinations are given in the Supporting Information. The structures were solved by direct methods (*SHELXS97*[35]), and developed by full least-squares refinement on F^2 (*SHELXL97*[35]). Crystallographic figures were prepared using *XSEED*,[36] and coordination volumes (V_{Oh}) were calculated using *Olex2*.[37]

Other measurements

Electrospray mass spectra (MS) were obtained on a Bruker MicroTOF spectrometer, from from chloroform (organic ligands) or acetonitrile (metal complexes) solution. Sodium cations and formate anions in the molecular ion assignments originate from calibrants in the spectrometer feed solutions. CHN microanalyses were performed by the University of Leeds School of Chemistry microanalytical service, or the London Metropolitan University microanalytical service. X-ray powder diffraction patterns were measured using a Bruker D2 Phaser diffractometer, with Cu-K_α radiation (λ = 1.5418 Å). Magnetic susceptibility measurements were obtained using a Quantum Design SQUID magnetometer in an applied field of 5000 G. Diamagnetic corrections were estimated from Pascal's constants,[38] and a diamagnetic correction for the sample holder was also applied. Magnetochemical calculations and graph preparation were carried out using *SIGMAPLOT*.[39] Susceptibility measurements in solution were obtained by Evans method using a Bruker DRX500 spectrometer operating at 500.13 MHz.[40] A diamagnetic correction for the sample,[38] and a correction for the variation of the density of the CD_3CN solvent with temperature,[41] were applied to these data.

DFT calculations were performed using *SPARTAN'16* for *Windows*,[42] with the B86PW91 functional and def-SVP2 basis set. Low spin systems were treated as spin restricted and high spin systems spin unrestricted. The calculations were performed in the gas phase, since a solvent gradient for iron was not implemented in *SPARTAN'16* at the time of writing. The atomic coordinates for $[Fe(bpp)_2]^{2+}$ in the high-spin and low-spin crystal structures of $[Fe(bpp)_2][BF_4]_2$[43] were used as the starting point for the undistorted geometry minimizations, with ligand C atoms replaced by N atoms as appropriate for each complex. The Jahn-Teller distorted geometry minimizations also started from crystallographic models, with the *trans*-N{triazine}–Fe–N{triazine} angle (ϕ in Table 1, see below[44]) fixed at a series of different values. This was necessary to prevent the molecules relaxing back towards their undistorted conformations, which represent the global minimum structures under this computational protocol.

Results and Discussion

Our initial approach towards substituted bpt derivatives (Chart 2) was to prepare 2,4-di(pyrazol-1-yl)-6-chloro-1,3,5-triazine (L^1) through treatment of cyanuric chloride with 2 equiv pyrazole, in the presence of NaH or NEt_3 as base.[34] However, as previously reported,[28] the major product from such reactions was often trisubstituted 2,4,6-tri(pyrazol-1-yl)-1,3,5-triazine (L^2). Analogous reactions using different pyrazole precursors afforded a number of other *tris*-pyrazolyl-1,3,5-triazine derivatives, whose solubility was found to depend strongly on the pyrazole substitution pattern. Of these, 2,4,6-tri(3,5-dimethylpyrazol-1-yl)-1,3,5-triazine (L^3)[33] and 2,4,6-tri(4,5,6,7-tetrahydroindazol-2-yl)-1,3,5-triazine (L^4) proved soluble enough for complexation studies.

L^1 was ultimately obtained by a similar procedure without the addition of base, but the yield was too low and unreliable for L^1 to be a convenient starting material for other bpt ligands. The new ligands 2,4-di(pyrazol-1-yl)-6-dimethylamino-1,3,5-triazine (L^5) and 2,4-di(pyrazol-1-yl)-6-isopropylsufanyl-1,3,5-triazine (L^8) were obtained instead by treatment of L^2 with dimethylamine or sodium propan-2-thiolate, respectively. 2,4-Di(pyrazol-1-yl)-6-diethylamino-1,3,5-triazine (L^6) was also prepared, by the literature procedure,[28] but 2,4-di(pyrazol-1-yl)-6-ethoxy-1,3,5-triazine (L^7) was not obtained as a free organic in this work (see below). The identities of L^1, L^3-L^6 and L^8 were confirmed by crystal structure determinations. Our structure of L^3 (monoclinic, space group $P2_1/n$) is a different polymorph from the published structure of this compound (orthorhombic, $Pna2_1$).[45]

Homoleptic iron(II) complexes of all the isolated ligands, except L^1, were prepared by treating them with 0.5 equiv $Fe[BF_4]_2{\cdot}6H_2O$ in aprotic solvents. The complexes were isolated as yellow or orange solids following the usual work-up. A similar product was obtained from complexation reactions involving L^1, but attempts to recrystallize this material did not afford $[Fe(L^1)_2][BF_4]_2$ in pure form. Insight into this was provided when L^1 and $Fe[BF_4]_2{\cdot}6H_2O$ were reacted in ethanol, which precipitated $[Fe(L^7)_2][BF_4]_2$ in analytical purity. Apparently, coordination of L^1 to a Lewis acidic metal ion activates its chloro substituent to nucleophilic attack by ethanol, and presumably by other exogenous nucleophiles. That is consistent with previous reports, where bpt derivatives have been activated to hydrolysis by metal coordination.[46] A black byproduct was sometimes noted during the synthesis of $[Fe(L^6)_2][BF_4]_2$, which was identified as the corresponding iron(III) complex. This was prepared in pure form as its perchlorate salt, by treating $Fe[ClO_4]_3{\cdot}nH_2O$ with 2 equiv L^6 as before.

All the iron(II) complexes were characterized crystallographically. Two solvent-free polymorphs of $[Fe(L^2)_2][BF_4]_2$ were characterized of which one, α-$[Fe(L^2)_2][BF_4]_2$ (cubic, space group $Ia\bar{3}d$), exhibits extensive symmetry-imposed disorder. The asymmetric unit contains one-third of a L^2 ligand, spanning a crystallographic three-fold axis. The iron atom is disordered by symmetry across all three binding pockets of the ligand, with the unique L^2 pyrazolyl group similarly disordered about a two-fold axis (Figure 1). Each metal ion coordinates two symmetry-related ligands, in a distorted six-coordinate geometry with crystallographic $\bar{4}$ symmetry (Figure 2). Since each ligand can only bind one iron atom, the model is best interpreted as a cubic array of L^2 ligands linked in pairwise fashion by a random distribution of iron atoms through the lattice. The second polymorph β-$[Fe(L^2)_2][BF_4]_2$ (tetragonal, $I4_1/acd$) does not have such metal ion disorder, but also contains a $\bar{4}$-symmetric cation whose pendant pyrazolyl groups are disordered about a C_2 axis. The α polymorph was most commonly found in crystallization vials, and also appears to dominate in bulk samples of $[Fe(L^2)_2][BF_4]_2$ by powder diffraction (Figure S14).[47]

The other complex structures are crystallographically more routine (Figure 2). The complex cations in $[Fe(L^3)_2][BF_4]_2\cdot 2CH_2Cl_2$, $[Fe(L^5)_2][BF_4]_2\cdot {}^1/_2CH_3CN$ and $[Fe(L^7)_2][BF_4]_2$ have internal crystallographic C_2 symmetry. Two pseudo-polymorphs $[Fe(L^6)_2][BF_4]_2\cdot n CH_2Cl_2$ ($n \approx 0.57$) and $[Fe(L^6)_2][BF_4]_2\cdot {}^1/_2CH_2Cl_2$ were also analyzed, which respectively contain three or two crystallographically unique molecules with small differences in their coordination geometries (see below). None of these compounds is isostructural with the corresponding complex from the $[Fe(bpp)_2]^{2+}$ series with the same 'R^1' pyridyl substituents (Chart 1), where the comparison can be made.[12,13,48] All the crystalline compounds are high-spin at 100-120 K, according to their metric parameters (Table 1).[44,49,50] That includes disordered α-$[Fe(L^2)_2][BF_4]_2$, whose Fe–N

distances are ambiguous but which is clearly high-spin from the angular parameters in the Table.[44] This was confirmed by the volume of the FeN_6 coordination octahedron (V_{Oh}) in each molecule, which takes values between 12.0-12.5 $Å^3$. For comparison, derivatives of $[Fe(bpp)_2]^{2+}$ exhibit $11.4 \leq V_{Oh} \leq 13.0$ when high-spin, and $9.2 \leq V_{Oh} \leq 9.9$ in their low-spin forms (Table S4).

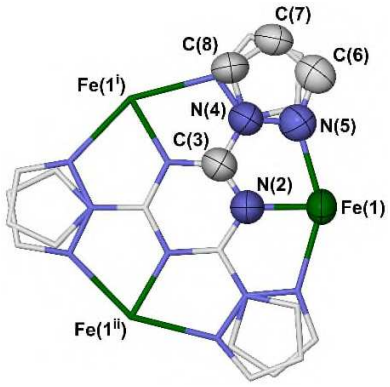

Figure 1. View of the ligand and metal ion disorder in the structure of α-$[Fe(L^2)_2][BF_4]_2$. The atoms in the asymmetric unit are shown with 50 % displacement ellipsoids, while their symmetry equivalent disorder sites have arbitrary radii. H atoms have been omitted for clarity. Symmetry codes: (i) $^1/_4–z$, $^1/_4–y$, $^1/_4–x$; (ii) z, x, y. Color code: C, white; Fe, green; N, blue.

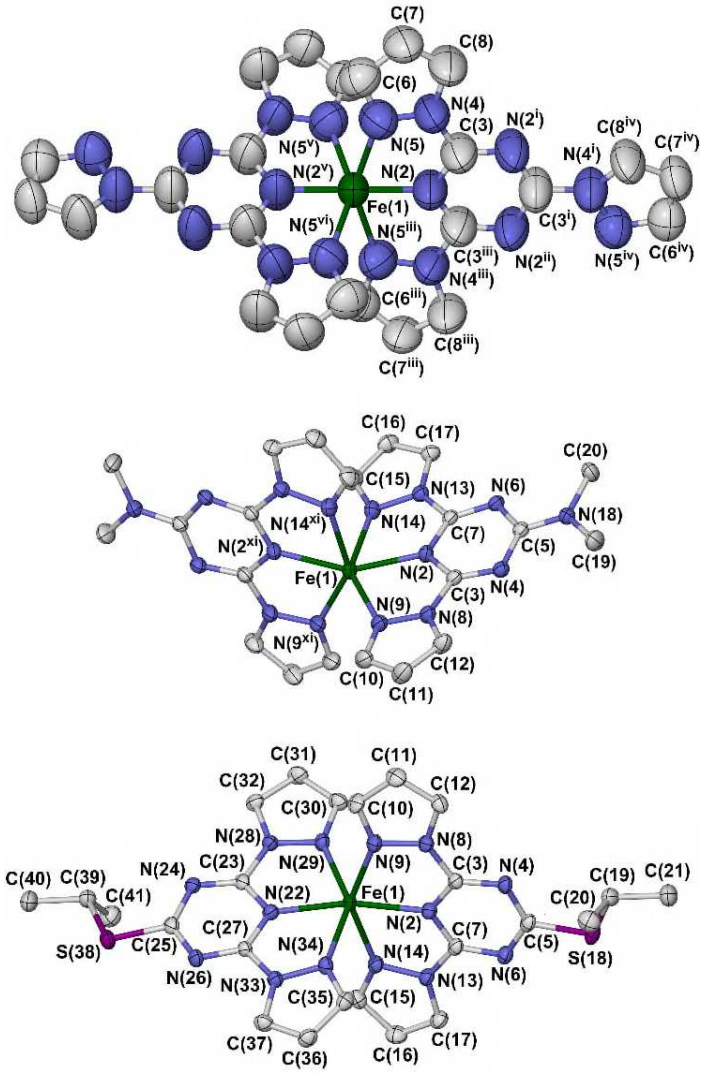

Figure 2. Views of the complex dications in the crystal structures of α-$[Fe(L^2)_2][BF_4]_2$ (top), $[Fe(L^5)_2][BF_4]_2 \cdot {}^1/_2CH_3CN$ (center) and $[Fe(L^8)_2][BF_4]_2$ (bottom). Displacement ellipsoids are at the 50 % probability level, and H atoms have been omitted for clarity. Symmetry codes: (i) ${}^1/_4-z$, ${}^1/_4-y$, ${}^1/_4-x$; (ii) z, x, y; (iii) ${}^1/_4-x$, ${}^1/_4-z$, ${}^1/_4-y$; (iv) ${}^1/_4-y$, ${}^1/_4-x$, ${}^1/_4-z$; (v) x, $-y$, ${}^1/_2-z$; (vi) ${}^1/_4-x$, $-{}^1/_4+z$, ${}^1/_4+y$; (xi) $-x$, ${}^1/_2-y$, z. Color code: C, white; Fe, green; N, blue; S, purple.

Table 1 Selected metric parameters for the complexes in this work (Å, Å^3, º).[44] A more detailed bond length and angle Table for these structures is given in Table S3.

	α-$[Fe(L^2)_2][BF_4]_2$[a]	β-$[Fe(L^2)_2][BF_4]_2$[a]	$[Fe(L^3)_2][BF_4]_2\cdot 2CH_2Cl_2$[b]	$[Fe(L^4)_2][BF_4]_2\cdot 1.55CH_3CN\cdot 0.45CH_2Cl_2$
Fe−N{triazinyl}	1.911(3)	2.097(5)	2.099(2)	2.093(2), 2.099(2)
Fe−N{pyrazolyl}	2.279(11)	2.224(3)	2.192(2), 2.257(2)	2.188(2)-2.301(3)
V_{Oh}	12.15(5)	12.358(14)	11.972(10)	12.495(9)
Σ	176.6(19)	177.8(4)	174.8(3)	166.5(3)
Θ	489	510	556	522
ϕ	180	180	159.62(13)	166.10(10)
θ	69.79(15)	71.89(3)	86.20(2)	82.78(3)
	$[Fe(L^5)_2][BF_4]_2\cdot {}^1/_2CH_3CN$[b]	$[Fe(L^6)_2][BF_4]_2\cdot nCH_2Cl_2$[c] Molecule A[d]	Molecule B	Molecule C
Fe−N{triazinyl}	2.109(2)	2.073(4)-2.151(10)	2.078(4), 2.083(4)	2.099(4), 2.102(4)
Fe−N{pyrazolyl}	2.219(3), 2.269(3)	2.188(8)-2.285(12)	2.223(4)-2.270(4)	2.215(4)-2.258(4)
V_{Oh}	12.104(10)	12.43(2)/12.54(2)	12.459(14)	12.299(14)
Σ	174.3(4)	151.8(12)/165.9(10)	163.6(5)	167.8(5)
Θ	541	485/520	510	532
ϕ	154.19(14)	168.3(4)/168.9(3)	168.60(14)	163.71(15)
θ	80.55(3)	85.12(7)/83.53(6)	81.33(4)	86.31(4)

Table 1 continued

	$[Fe(L^6)_2][BF_4]_2 \cdot {}^1/_2CH_2Cl_2$[e] Molecule A	Molecule B	$[Fe(L^7)_2][BF_4]_2$[b]	$[Fe(L^8)_2][BF_4]_2$
Fe−N{triazinyl}	2.0791(16), 2.0910(16)	2.0825(17), 2.0907(16)	2.0967(18)	2.087(4), 2.102(4)
Fe−N{pyrazolyl}	2.2141(17)-2.2474(17)	2.2040(17)-2.2605(17)	2.2048(19), 2.2147(19)	2.206(4)-2.244(4)
V_{Oh}	12.375(6)	12.446(6)	12.106(8)	12.283(16)
Σ	175.2(2)	162.5(2)	171.6(3)	166.8(3)
Θ	509	507	513	507
ϕ	173.54(7)	171.79(7)	168.75(10)	167.51(16)
θ	73.58(2)	80.24(2)	73.01(2)	75.24(5)

[a]The asymmetric unit of this compound contains one-quarter of a complex molecule, with crystallographic $\bar{4}$ symmetry. [b]The asymmetric unit of this compound contains half a complex molecule, with crystallographic C_2 symmetry. [c]There are three unique molecules in the asymmetric unit of this compound, labelled A-C. [d]This molecule suffers from whole-ligand disorder (Figure S10). [e]There are two unique molecules in the asymmetric unit of this compound, labelled A and B.

The FeN_6 donor spheres in the complexes all deviate significantly from the idealized D_{2d} symmetry for a $[Fe(bpt)_2]^{2+}$-type molecule (Figure 2). This is evident in the *trans*-N(triazine)–Fe–N(triazine) angle (ϕ, Table 1); and the dihedral angle between the least squares planes of the ligands in the complex (θ). An ideal D_{2d}-symmetric complex would have $\phi = 180°$ and $\theta = 90°$. However, these compounds show reduced values for at least one of these parameters, with $154.15(14) \leq \phi \leq 180°$ and $70.50(18) \leq \theta \leq 86.31(4)°$. Such distorted geometries are also well-known in high-spin complexes from the $[Fe(bpp)_2]^{2+}$ family,[11,12] and reflect a Jahn-Teller splitting of the high-spin $^5T_2$ configuration.[43] This causes a distortion towards a trigonal prismatic coordination geometry, that is constrained by the bpp (or bpt) ligand bite angle.[12] The Jahn-Teller distortion is specific to the high-spin state, and low-spin complexes of this type adopt more regular coordination geometries. Thus, crystalline $[Fe(bpp)_2]^{2+}$ derivatives with reduced values of ϕ and θ can be kinetically trapped in their high-spin form by the rigid lattice, that cannot accommodate the structure rearrangement towards the undistorted low-spin state.[43,51]

In practise, SCO in high-spin $[Fe(bpp)_2]^{2+}$ derivatives becomes progressively rarer as the deviation of ϕ from 180°, and of θ from 90°, increases.[11,52] On that basis, the compounds in this study all adopt coordination geometries that should disfavor or prohibit SCO (Figure 3). However, such geometric inhibition of SCO in the solid state has no relevance to the observation of SCO in solutions of the complexes,[13,53] presumably because distorted and undistorted forms of the high-spin complexes interconvert rapidly in a fluid medium (see below).

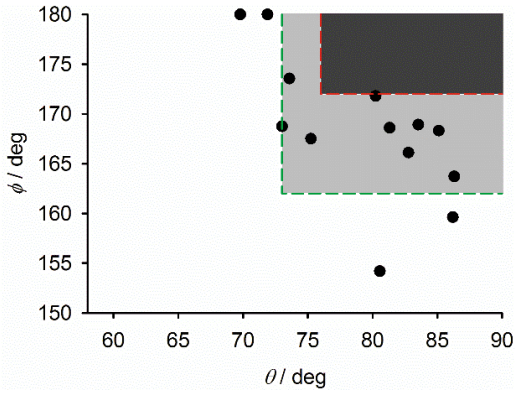

Figure 3. The deviation of the crystalline complexes in this work from idealized D_{2d} symmetry, as measured by ϕ and θ (Table 1). The axes are scaled to the range of values found in $[Fe(bpp)_2]^{2+}$ derivatives.[11] High-spin complexes in the shaded regions of the graph commonly (dark gray) or rarely (pale gray) exhibit SCO on cooling.[48,52] High-spin $[Fe(bpp)_2]^{2+}$ derivatives in the unshaded part of the graph never undergo SCO in the solid state.

Except for $[Fe(L^3)_2][BF_4]_2$, whose solvated crystals collapse to an amorphous powder upon drying, bulk samples of the mononuclear complexes are phase pure and isostructural with the crystalline phases by X-ray powder diffraction (Figure S14). Magnetic susceptibility measurements confirmed that all the solid iron(II) compounds remain high-spin on cooling between 3-300 K (Figure S15), which is consistent with their crystal structures. All these data show the expected decrease in $\chi_M T$ below 50 K, which arises from zero-field splitting of their high-spin state.[54] However, the magnitude of the low-temperature decrease differs somewhat between the compounds, implying that the zero-field splitting parameter D shows some variation across the series. That is consistent with our previous work on $[Fe(bpp)_2]^{2+}$ derivatives, where we have shown that complexes exhibiting large structural Jahn-Teller distortions have reduced

values of in D in the solid state.[55] Solid $[Fe(L^6)_2][ClO_4]_3$ is also high-spin at room temperature and below according to magnetic susceptibility data (Figure S15).

Electrospray mass spectra (ESMS) of all the complexes from MeCN are dominated by mononuclear species, with $[FeL_2]^{2+}$ (L = L^2-L^8) the most intense peak in each case. Notably, some spectra also contained ions assignable to species containing 2,4-dipyrazolyl-6-hydroxo-1,3,5-triazine (Chart 1, R^1 = OH) or, for $[Fe(L^8)_2][BF_4]_2$, 2,4-dipyrazolyl-1,3,5-triazine-6-thiol (R^1 = SH). These will arise from ligand hydrolysis reactions inside the spectrometer (Figure S17).[46] ^{1}H NMR spectra for all the complexes in CD_3NO_2 at 298 K all showed just one contact-shifted ligand environment with C_2 or m symmetry; there were no peaks in the diamagnetic region to indicate the presence of uncoordinated ligand (Figure S18). In contrast, the ^{1}H NMR spectra of $[Fe(L^2)_2][BF_4]_2$ and $[Fe(L^8)_2][BF_4]_2$ in CD_3CN were severely broadened, which may also reflect ligand exchange processes in this more nucleophilic solvent. ^{1}H NMR spectra of the other complexes in CD_3CN resembled those in CD_3NO_2. For $[Fe(L^3)_2][BF_4]_2$ only, at least two significant paramagnetic impurities were clear in both solvents, comprising 10-30 % of the sample. These may again indicate ligand exchange reactions, occurring more slowly than the other complexes; and/or, *in situ* hydrolysis of the L^3 ligand which was evident in the mass spectrum of this complex (see above).[46]

The contact shifts of the C–H groups in the metal-coordinated pyrazolyl rings are very similar for all the complexes, implying they have similar magnetic moments under these conditions. Variable temperature magnetic measurements on three of the complexes in CD_3CN confirmed their high-spin nature, with no onset of SCO being observed within the liquid range of the solvent (Figure S16). Hence, the high-spin nature of the complexes in the solid state is not

simply imposed by their coordination geometry,[43,51] but genuinely reflects the weak ligand field imposed by the bpt ligand donors.

Many compounds from the $[Fe(bpp)_2]^{2+}$ [11,12] and $[Fe(bpyz)_2]^{2+}$ [20,21] families, and the only published $[Fe(bpym)_2]^{2+}$ derivative,[22] exhibit thermal SCO in the solid state. Moreover, $[Fe(bpp)_2]^{2+}$ and $[Fe(bpyz)_2]^{2+}$ derivatives often undergo SCO in solution near room temperature.[13,21] Hence, the consistently high-spin nature of the mononuclear complexes in this work was unexpected. To rationalize this result, gas phase DFT calculations were performed on the four prototypical complexes from this series (Chart 1, $R^1 = R^2 = H$), with $[Fe(bpt)_2]^{2+}$ being included as a model for the $[FeL_2]^{2+}$ ($L = L^2$-L^8) derivatives in this work. The calculations used the B86PW91 functional and def-SVP2 basis set. These were chosen as the closest analogues available in *SPARTAN'16*[42] of the BP86/def-SVP2 functional/basis set combination, which performed well in other calculations of comparative spin state energies in iron compounds,[13,56] including a series of $[Fe(bpp)_2]^{2+}$ derivatives.[13] The metal-free ligands were also calculated, in the all *cisoid* conformation required for metal ion coordination.

The complexes were first minimized in geometries that would be consistent with SCO, with only minor deviations from ideal D_{2d} symmetry.[11,43,52] For $[Fe(bpp)_2]^{2+}$ [43] and $[Fe(bpyz)_2]^{2+}$,[20] the average Fe–N bond lengths to the pyridyl/pyrazinyl and pyrazolyl donors in the calculated low-spin structures agree with the experimental values to within the crystallographic experimental error (Tables 2 and S7). In contrast the computed high-spin Fe–N distances are longer than the experimental values, with the discrepancy being greater for $[Fe(bpyz)_2]^{2+}$ (1.2-1.3 % longer) than for $[Fe(bpp)_2]^{2+}$ (0.2-0.7 % longer). That is still a good level of agreement for a calculation of this type, however.

Table 2 Computed average Fe–N bond lengths (Å) and ligand bite angles (α, °) for the iron(II) complexes of the ligands in Chart 1 ($R^1 = R^2 = H$), in their undistorted coordination geometries. Available crystallographic data are also included in square brackets for comparison.[20,43] A more complete list of bond lengths and angles for these computed structures is in Table S6.

	Spin state[a]	Fe−N{azinyl}$_{av}$	Fe−N{pyrazolyl}$_{av}$	α
$[Fe(bpp)_2]^{2+}$	LS	1.905 [1.907(2)]	1.980 [1.983(4)]	80.2 [80.08(14)]
	HS	2.156 [2.140(2)]	2.202 [2.198(4)]	73.3 [73.42(13)]
$[Fe(bpyz)_2]^{2+}$	LS	1.893 [1.894(4)]	1.988 [1.985(6)]	80.0 [79.7(2)]
	HS	2.145 [2.119(4)]	2.214 [2.185(6)]	73.1 [73.3(2)]
$[Fe(bpym)_2]^{2+}$	LS	1.893	1.995	79.6
	HS	2.134	2.230	72.9
$[Fe(bpt)_2]^{2+}$	LS	1.880	2.013	78.9
	HS	2.108	2.263	72.5

[a]LS = low-spin, HS = high-spin.

A low-spin ground state was computed for all the complexes, which may reflect the tendency of pure density functionals like B86PW91 to overstabilize the low-spin state.[57] However the energy difference between the high-spin and low-spin states, relative to $[Fe(bpp)_2]^{2+}$ [ΔE_{rel}(HS-LS), Table 3], shows a pronounced stabilization of the high-spin state in the order:

$$[Fe(bpp)_2]^{2+} \approx [Fe(bpyz)_2]^{2+} < [Fe(bpym)_2]^{2+} < [Fe(bpt)_2]^{2+}$$

That reproduces the experimental observation that $[Fe(bpt)_2]^{2+}$ shows the greatest tendency within this series to adopt the high-spin form.

Table 3 Computed energies of the high-spin (HS) and low-spin (LS) states of iron(II) complexes of the ligands in Chart 1 ($R^1 = R^2 = H$), in their undistorted coordination geometries. ΔE_{rel}(HS-LS) is the energy difference between the high- and low-spin states, relative to $[Fe(bpp)_2]^{2+}$.

	E(HS), Ha	*E*(LS), Ha	ΔE_{rel}(HS-LS), kcalmol^{-1}
$[Fe(bpp)_2]^{2+}$	–2659.474752	–2659.500527	0
$[Fe(bpyz)_2]^{2+}$	–2691.493297	–2691.518815	–0.2
$[Fe(bpym)_2]^{2+}$	–2691.530611	–2691.552588	–2.4
$[Fe(bpt)_2]^{2+}$	–2723.588339	–2723.605914	–5.2
$[Fe(tpp)_2]^{2+}$ [a]	–3109.343628	–3109.367359	–1.3
$[Fe(L^2)_2]^{2+}$	–3173.478556	–3173.494152	–6.4
$[Fe(bpp^{NMe2})_2]^{2+}$ [a]	–2927.349239	–2927.371824	–2.0
$[Fe(L^5)_2]^{2+}$	–2991.51927	–2991.533044	–7.5
$[Fe(bpp^{SiPr})_2]^{2+}$ [a]	–3691.507623	–3691.531936	–0.9
$[Fe(L^8)_2]^{2+}$	–3755.650716	–3755.666334	–6.4

[a]tpp = 2,4,6-tri(pyrazol-1-yl)pyridine; bpp^{NMe2} = 2,6-di(pyrazol-1-yl)-4-dimethylaminopyridine; bpp^{SiPr} = 2,6-di(pyrazol-1-yl)-4-isopropylsulfanylpyridine.

Consideration of the MOs for the low-spin complexes shows a similar sequence of metal- and ligand-based frontier orbitals for all the complexes (Figure 4). The magnitude of Δ_{oct} [in kcalmol^{-1}],[58] calculated from the *d*-orbital energies in each compound, follows the sequence:

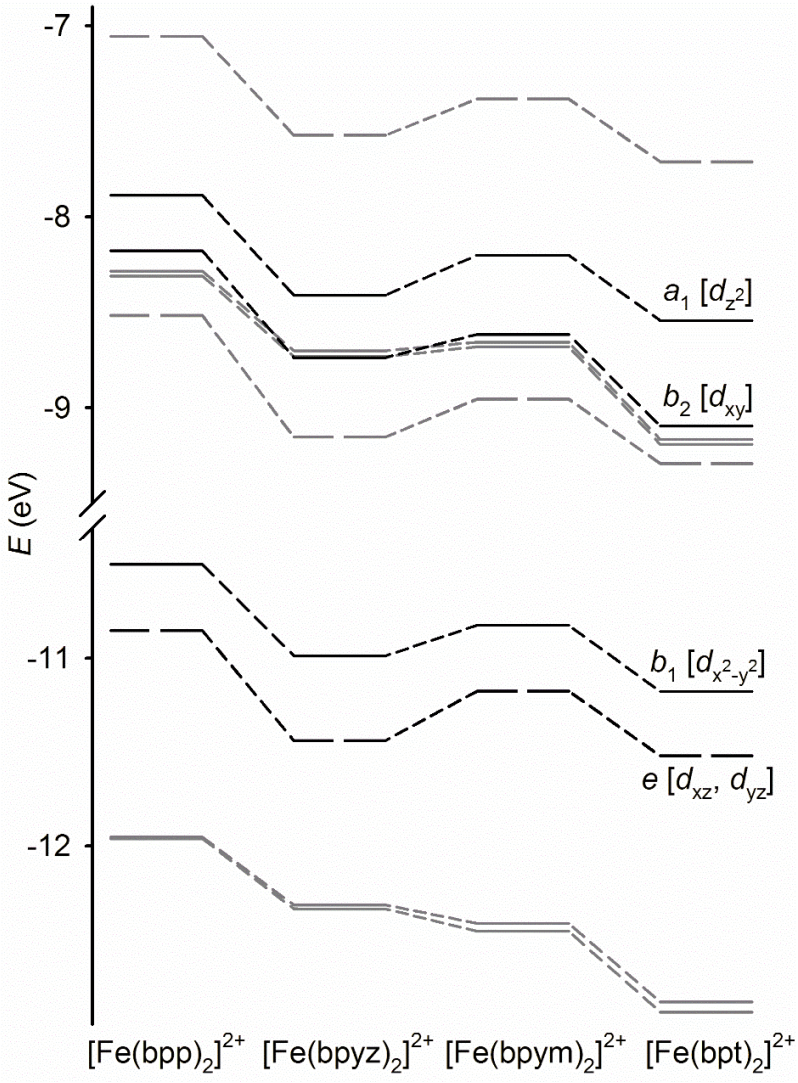

Figure 4. Computed frontier orbital energies for the low-spin forms of the complexes in this work.[58] Ligand-based MOs are de-emphasized for clarity.

$[Fe(bpyz)_2]^{2+}$ (62.6) ≈ $[Fe(bpp)_2]^{2+}$ (62.3) > $[Fe(bpym)_2]^{2+}$ (61.1) > $[Fe(bpt)_2]^{2+}$ (59.6)

While these values will also be overestimated,[57] the significantly weaker ligand field computed for $[Fe(bpt)_2]^{2+}$ is consistent with its more stable high-spin state. The greatest contributor to that trend in Δ_{oct} is an increased asymmetry of the σ-ligand field across that series, as shown by the

energy gap between the d_{xy} and d_{z2} orbitals which is almost twice as large in $[Fe(bpt)_2]^{2+}$ as in $[Fe(bpp)_2]^{2+}$ (Figure 5).[58] That predominantly reflects a greater stabilization of the d_{xy} orbital in $[Fe(bpym)_2]^{2+}$ and $[Fe(bpt)_2]^{2+}$, compared to the other *d*-orbitals whose energies vary more consistently between the compounds. Thus, the reduced ligand field in $[Fe(bpt)_2]^{2+}$ is caused by a weakening of the distal Fe–N{pyrazolyl} σ-bonds, which lie near the *xy* plane of the complex, rather than the Fe–N{triazinyl} σ-bonds oriented along the *z* axis.

Calculations of the free ligands reveal three MOs assignable to the coordinating lone pairs, with the azinyl-centered lone pair orbital lying 0.6-0.7 eV above the two pyrazole lone pair combinations (Figure S20). While the analysis is complicated by mixing of coordinating and peripheral lone pairs, the energy gap between these azinyl and pyrazolyl lone pair MOs follows the trend bpp ≈ bpym > btz > bpyz (Figure S21). That does not mirror the trends in Δ_{oct} or ligand field asymmetry for the complexes, described in the previous paragraph. Hence, variations in the lone pair orbital energies of the uncoordinated ligands cannot obviously be used to explain these observations. Rather, a geometric origin for the spin state trends is suggested by the computed metal–ligand bond lengths, which show a small but consistent contraction of the Fe–N{azinyl} bonds and lengthening of the Fe–N{pyrazolyl} bonds as the N content of the ligands increases (Table 2). This is accompanied by a narrowing of the ligand bite angle (α; Table 2, Figure 5), from 80.2° in $[Fe(bpp)_2]^{2+}$ to 78.9° in $[Fe(bpt)_2]^{2+}$ in the low-spin forms or from 73.3° to 72.5° in their high-spin states.[59] A lower bite angle would weaken the overlap of the pyrazolyl *N*-donors with the metal d_{xy} orbital in $[Fe(bpym)_2]^{2+}$ and $[Fe(bpt)_2]^{2+}$, as observed (Figure 4).

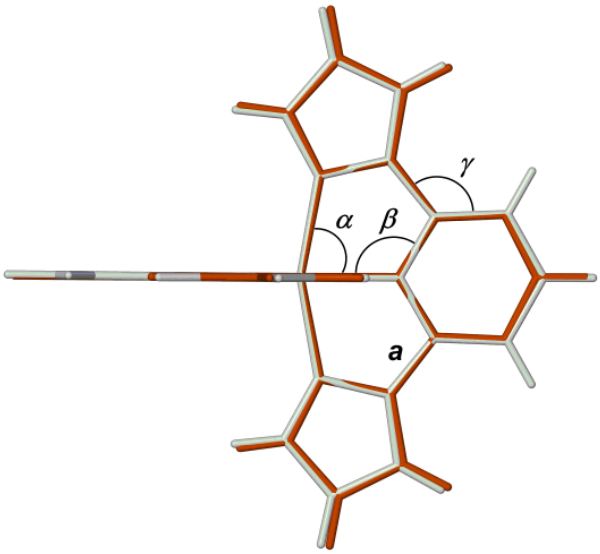

Figure 5. Overlaid DFT-minimized structures of undistorted, low-spin $[Fe(bpp)_2]^{2+}$ (white) and $[Fe(bpt)_2]^{2+}$ (orange), showing the ligand bite angle (α). The parameters contributing to the smaller value of α in $[Fe(bpt)_2]^{2+}$ are highlighted, and discussed in the text.

Two geometric factors contribute to the different bite angles in the complexes. First, is the more compact triazine ring in bpt, compared to the pyridyl ring in bpp (each extra C–N bond in bpt is 0.05 Å shorter than the corresponding C–C bond in bpp[60]). This is reflected in the β angle (Figure 5), which is 2.3° larger in low-spin $[Fe(bpt)_2]^{2+}$ than in $[Fe(bpp)_2]^{2+}$; and in γ (Figure 5), which is 2.4° smaller in $[Fe(bpt)_2]^{2+}$. Both these differences indicate a widening of the five-membered chelate rings in coordinated bpt compared to bpp (the other internal angles in the chelate rings are equal to ±0.4° in the two complexes). Second is the C{azinyl}–N{pyrazolyl} bond length in the ligands (*a* in Figure 5), which becomes shorter as the N content of the ligand increases. Thus, *a* is computed to be 1.405 Å in $[Fe(bpp)_2]^{2+}$ but 1.393 Å in $[Fe(bpt)_2]^{2+}$. That

difference appears to be reproduced crystallographically; for example, *a* is 1.406(1) Å and 1.393(4) Å in the crystal structures of bpp and L^2, respectively.[61]

The generality of these results was probed with three pairs of complexes from the $[Fe(bpp)_2]^{2+}$ and $[Fe(bpt)_2]^{2+}$ families with identical R^1 substitutents (Chart 1; R^1 = pyrazol-1-yl, NMe_2 and S*i*Pr; R^2 = H), which were calculated in approximately D_{2d}-symmetric coordination geometries as before. The stabilization of the high-spin state in both series of compounds follows the trend: R^1 = H < pyrazolyl ≈ S*i*Pr < NMe_2 (Table 3), which is consistent with our previous study of substituent effects in the $[Fe(bpp)_2]^{2+}$ series.[13] The high-spin state of $[Fe(L^2)_2]^{2+}$, $[Fe(L^5)_2]^{2+}$ and $[Fe(L^8)_2]^{2+}$ is consistently preferred by 5.0-5.5 kcalmol^{-1} compared to the corresponding $[Fe(bpp)_2]^{2+}$ derivative. These minimized molecular structures show same structural trends described above; that is, the $[Fe(bpt)_2]^{2+}$ derivatives show shorter Fe–N{azinyl} bonds, longer Fe–N{pyrazolyl} bonds and narrower ligand bite angles than the corresponding $[Fe(bpp)_2]^{2+}$ complexes, with the differences being more pronounced in the low-spin states (Table S9).[59]

Finally, all the $[Fe(bpt)_2]^{2+}$ derivatives in this work adopt significant angular Jahn-Teller distortions in the crystalline phase (Table 1, Figure 4). Hence, an alternative explanation for the high-spin state of solid $[Fe(bpt)_2]^{2+}$ derivatives might be that they show a greater propensity to form Jahn-Teller distorted high-spin geometries than complexes of the other ligand types in Chart 1. This was probed by minimizing high-spin $[Fe(bpp)_2]^{2+}$ and $[Fe(bpt)_2]^{2+}$ in three distorted geometries with fixed values of $155 \leq \phi \leq 165°$.[62] The distorted molecules lie ≤1.1 kcalmol^{-1} above the corresponding undistorted structures, or ≤0.6 kcalmol^{-1} when $\phi \geq 160°$ (Table 4). These values confirm the shallow nature of the distortion potential surface, and are consistent with previous computational studies of $[Fe(bpp)_2]^{2+}$.[43,51] The additional distortion energy, ΔE(dist), is up to 45 % smaller for $[Fe(bpt)_2]^{2+}$ compared to $[Fe(bpp)_2]^{2+}$ at each value of ϕ, with

the difference between them being reduced at larger distortions (Table 4). However, since the distortion energies are of the order of kT (0.6 kcalmol^{-1} at 293 K), both compounds should contain comparable populations of distorted high-spin molecules under ambient conditions. We conclude that the distorted coordination geometries adopted by crystalline [FeL_2][BF$_4$]$_2$ (L = L^2-L^8) reflect the high-spin nature of the [Fe(bpt)$_2$]$^{2+}$ centre, but do not cause it.

Table 4 Computed energies for the minimized Jahn-Teller distorted geometries of high-spin [Fe(bpp)$_2$]$^{2+}$ and [Fe(bpt)$_2$]$^{2+}$ (Figure S25 and Table S11).[62] ΔE(dist) is their energy relative to the corresponding undistorted molecule (Table 3).

	ϕ (°)[a]	θ (°)	E, Ha	ΔE(dist), kcalmol^{-1}
[Fe(bpp)$_2$]$^{2+}$	165	84.5	–2659.474234	+0.3
	160	82.7	–2659.473856	+0.6
	155	81.0	–2659.472979	+1.1
[Fe(bpt)$_2$]$^{2+}$	165	83.9	–2723.588053	+0.2
	160	82.7	–2723.587634	+0.4
	155	81.9	–2723.586706	+1.0

[a]This parameter was fixed during the geometry minimizations.

Conclusions

Homoleptic $Fe[BF_4]_2$ complexes of seven bpt derivatives have been characterized by structural and magnetochemical methods. The complexes are all high-spin in the solid state and, where measured, in solution regardless of the substituents on the pyrazolyl or triazinyl rings. This was unexpected for three reasons. First, many analogous complexes from the $[Fe(bpp)_2]^{2+}$,[11,12] $[Fe(bpyz)_2]^{2+}$ [20,21] and $[Fe(bpym)_2]^{2+}$ [22] series (Chart 1) are SCO-active. Second, iron(II) complexes of some 2,4-di(pyrid-2-yl)-1,3,5-triazine derivatives also exhibit thermal SCO above room temperature, so tridentate ligands with triazinyl N-donor groups can support SCO in principle.[30] Lastly, previous work on the $[Fe(bpp)_2]^{2+}$ system concluded that ligands with electron-withdrawing 'R^1' substituents (Chart 1) favor the low-spin state of their complexes by promoting Fe→L π-back-donation.[13] That prediction extends to $[Fe(bpyz)_2]^{2+}$, whose pyrazinyl donors are less electron-rich than the pyridyl donors in bpp.[21] It does not apply to $[Fe(bpt)_2]^{2+}$ complexes, however, which are high-spin despite the strong π-acidity of the 1,3,5-triazinyl ring.[28,29]

DFT calculations reproduce the stabilization of the high-spin state in $[Fe(bpt)_2]^{2+}$ and its derivatives. Surprisingly, the computed molecular structures and *d*-orbital energies both imply that this does not reflect the electronic character of the 1,3,5-triazinyl donor group. Rather, the main contributor to this result is a weakening of the Fe–N{pyrazolyl} σ-bonding interaction in $[Fe(bpt)_2]^{2+}$, compared to the other complexes in the previous paragraph (Figure 5). The effect can be traced to the ligand bite angle, which is computed to be 1.3° narrower in $[Fe(bpt)_2]^{2+}$ than in $[Fe(bpp)_2]^{2+}$ in their low-spin forms. That reflects subtle geometric differences between the triazinyl and pyridyl rings in the two ligand types.

Stabilization of the high-spin state of a metal complex through the ligand conformation has been observed before in other complexes. For example, sterically induced twisting of a polypyridyl ligand forces its N-donor lone pairs out of the metal–ligand vector, thus weakening the Fe–N σ-bonds and affording high-spin complexes.[63] The high-spin nature of $[Fe(bpt)_2]^{2+}$ is a more subtle example of this phenomenon, that does not rely on steric crowding. Small changes to the ligand backbone, in a class of complex that already exhibits a small ligand bite angle, reduce the bite angle still further and in turn weaken the ligand field. A related correlation, between ligand geometry and metal ion spin state in homoleptic iron(II) di-imine complexes, has also been noted in another recent study.[64]

In conclusion, the spin state of a complex cannot always be predicted simply from the electronic and steric character of its ligand donors. Subtle geometric factors, such as the narrowing of a chelate ligand bite angle by *ca* 1° in this work, are enough to a produce a high-spin complex where a low-spin one might otherwise have been expected. Such considerations should be taken into account when designing complexes with specific spin state properties for applications in molecular magnetism or catalysis.[65]

ASSOCIATED CONTENT

Supporting Information The following material is available free of charge via the Internet at http://pubs.acs.org.

Experimental data, refinement procedures and tabulated metric parameters for the crystal structure determinations; X-ray powder diffraction, solid state and solution phase

magnetic susceptibility data; details of the minimized structures from the DFT calculations; V_{Oh} values for published derivatives of $[Fe(bpp)_2]^{2+}$, for comparison with those in Table 1 (PDF).

X-ray crystal structures of the organic ligands: CCDC 1504278–1504282 and 1546568 (CIF).

X-ray crystal structures of the metal complexes: CCDC 1502196, 1504283–1504289 and 1534692 (CIF).

Experimental data sets associated with this paper are available from the University of Leeds library (http://doi.org/10.5518/213).

AUTHOR INFORMATION

Corresponding Author

*Email: m.a.halcrow@leeds.ac.uk

Notes

The authors declare no competing financial interest.

ACKNOWLEDGMENT

This work was funded by the Leverhulme Trust (RPG-2015-095), and by the EPSRC (EP/K012576/1 and EP/K00512X/1). We thank Diamond Light Source for access to beamline I19 (MT10334) that contributed to the results presented here. The authors also thank Dr. O. Cespedes (School of Physcs and Astronomy, University of Leeds) and Mr. S. Barrett (School of Chemistry, University of Leeds) for help with the solid state and solution magnetic susceptibility measurements, respectively. Support by the COST network CM1305 *Explicit Control of Spin States in Technology and Biology* (ECOSTBio) is also gratefully acknowledged.

REFERENCES

(1) Gütlich, P.; Goodwin, H. A. (eds.) *Spin Crossover in Transition Metal Compounds I−III, Topics in Current Chemistry*; Springer-Verlag: Berlin, 2004; Vols. 233−235.

(2) Halcrow, M. A. (ed), *Spin-Crossover Materials - Properties and Applications,* John Wiley & Sons, Ltd.: New York, 2013, p. 568.

(3) For other recent general reviews of SCO chemistry see: (a) Gütlich, P. Spin Crossover – Quo Vadis? *Eur. J. Inorg. Chem.* **2013**, 581−591. (b) Gütlich, P.; Gaspar, A. B.; Garcia, Y. Spin State Switching in Iron Coordination Compounds. *Beilstein J. Org. Chem.* **2013**, *9*, 342−391. (c) Guionneau, P. Crystallography and Spin-Crossover. A View of Breathing Materials. *Dalton Trans.* **2014**, *43*, 382−393. (d) Brooker, S. Spin Crossover with Thermal Hysteresis: Practicalities and Lessons Learnt. *Chem. Soc. Rev.* **2015**, *44*, 2880−2892. (e) Sato, O. Dynamic Molecular Crystals with Switchable Physical Properties. *Nature Chem.* **2016**, *8*, 644–656. (f) Kumar, K. S.; Ruben, M. Emerging Trends in Spin Crossover (SCO) Based Functional Materials and Devices. *Coord. Chem. Rev.*, doi: 10.1016/j.ccr.2017.03.024

(4) Kahn, O.; Martinez, C. J. Spin-Transition Polymers: from Molecular Materials Toward Memory Devices. *Science* **1998**, *279*, 44–48.

(5) (a) Matsuda, M.; Tajima, H. Thin Film of a Spin Crossover Complex $[Fe(dpp)_2](BF_4)_2$. *Chem. Lett.* **2007**, *36*, 700–701. (b) Takahashi, K.; Cui, H.-B.; Okano, Y.; Kobayashi, H.; Mori, H.; Tajima, H.; Einaga, Y; Sato, O. Evidence of the Chemical Uniaxial Strain Effect on Electrical Conductivity in the Spin-Crossover Conducting Molecular System: $[Fe^{III}(qnal)_2][Pd(dmit)_2]_5\cdot$acetone. *J. Am. Chem. Soc.* **2008**, *130*, 6688–6689. (c) Rotaru, A.; Gural'skiy, I. A.; Molnár, G.; Salmon, L.; Demont, P.; Bousseksou, A. Spin State Dependence of

Electrical Conductivity of Spin Crossover Materials. *Chem. Commun.* **2012**, *48*, 4163–4165. (d) Phan, H.; Benjamin, S. M.; Steven, E.; Brooks, J. S.; Shatruk, M. Photomagnetic Response in Highly Conductive Iron(II) Spin-Crossover Complexes with TCNQ Radicals. *Angew. Chem. Int. Ed.* **2015**, *54*, 823–827. (e) Shvachko, Yu. N.; Starichenko, D. V.; Korolyov, A. V.; Yagubskii, E. B.; Kotov, A. I.; Buravov, L. I.; Lyssenko, K. A.; Zverev, V. N.; Simonov, S. V.; Zorina, L. V.; Shakirova, O. G.; Lavrenova, L. G. The Conducting Spin-Crossover Compound Combining Fe(II) Cation Complex with TCNQ in a Fractional Reduction State. *Inorg. Chem.* **2016**, *55*, 9121−9130.

(6) (a) Ni, Z.-P.; Liu, J.-L.; Hoque, M. N.; Liu, W.; Li, J.-Y.; Chen, Y.-C.; Tong, M.-L. Recent Advances in Guest Effects on Spin-Crossover Behavior in Hofmann-Type Metal-Organic Frameworks. *Coord. Chem. Rev.* **2017**, *335*, 28–43. (b) Ohtani, R.; Hayami, S. Guest-Dependent Spin-Transition Behavior of Porous Coordination Polymers. *Chem. Eur. J.* **2017**, *23*, 2236–2248.

(7) Manrique-Juárez, M. D.; Rat, S.; Salmon, L.; Molnár, G.; Quintero, C. M.; Nicu, L.; Shepherd, H. J.; Bousseksou, A. Switchable Molecule-Based Materials for Micro- and Nanoscale Actuating Applications: Achievements and Prospects. *Coord. Chem. Rev.* **2016**, *308*, 395–408.

(8) (a) Cavallini, M. Status and Perspectives in Thin Films and Patterning of Spin Crossover Compounds. *Phys. Chem. Chem. Phys.* **2012**, *14*, 11867−11876. (b) Shepherd, H. J.; Molnár, G.; Nicolazzi, W.; Salmon, L.; Bousseksou, A. Spin Crossover at the Nanometre Scale. *Eur. J. Inorg. Chem.* **2013**, 653–661. (c) Tissot, A. Photoswitchable Spin Crossover Nanoparticles. *New J. Chem.* **2014**, *38*, 1840–1845. (d) Lefter, C.; Davesne, V.; Salmon, L.; Molnár, G.; Demont, P.; Rotaru, A.; Bousseksou, A. Charge Transport and Electrical Properties of Spin Crossover Materials: Towards Nanoelectronic and Spintronic Devices. *Magnetochemistry* **2016**, *2*, 18/1–19.

(9) (a) Harzmann, G. D.; Frisenda, R.; van der Zant, H. S. J.; Mayor, M. Single-Molecule Spin Switch Based on Voltage-Triggered Distortion of the Coordination Sphere. *Angew. Chem. Int. Ed.* **2015**, *54*, 13425−13430. (b) Aragonès, A. C.; Aravena, D.; Cerdá, J. I.; Acís-Castillo, Z.; Li, H.; Real, J. A.; Sanz, F.; Hihath, J.; Ruiz, E.; Díez-Pérez, I. Large Conductance Switching in a Single-Molecule Device through Room Temperature Spin-Dependent Transport. *Nano Lett.* **2016**, *16*, 218−226.

(10) Halcrow, M. A. Structure:Function Relationships in Molecular Spin-Crossover Complexes. *Chem. Soc. Rev.* **2011**, *40*, 4119−4142.

(11) Halcrow, M. A. Iron(II) Complexes of 2,6-Di(pyrazol-1-yl)pyridines – a Versatile System for Spin-Crossover Research. *Coord. Chem. Rev.* **2009**, *253*, 2493–2514.

(12) Kershaw Cook, L. J.; Mohammed, R.; Sherborne, G.; Roberts, T. D.; Alvarez, S.; Halcrow, M. A. Spin State Behaviour of Iron(II)/Dipyrazolylpyridine Complexes. New Insights from Crystallographic and Solution Measurements. *Coord. Chem. Rev.* **2015**, *289–290*, 2–12.

(13) Kershaw Cook, L. J.; Kulmaczewski, R.; Mohammed, R.; Dudley, S.; Barrett, S. A.; Little, M. A.; Deeth, R. J.; Halcrow, M. A. A Unified Treatment of the Relationship Between Ligand Substituents and Spin State in a Family of Iron(II) Complexes. *Angew. Chem. Int. Ed.* **2016**, *55*, 4327–4331.

(14) (a) Secker, D.; Wagner, S.; Ballmann, S.; Härtle, R.; Thoss, M.; Weber, H. B. Resonant Vibrations, Peak Broadening, and Noise in Single Molecule Contacts: The Nature of the First Conductance Peak. *Phys. Rev. Lett.* **2011**, *106*, 136807/1–4. (b) Meded, V.; Bagrets, A.; Fink, K.; Chandrasekar, R.; Ruben, M.; Evers, F.; Bernand-Mantel, A.; Seldenthuis, J. S.; Beukman, A.; van der Zant, H. S. J. Electrical Control over the Fe(II) Spin Crossover in a Single Molecule:

Theory and Experiment. *Phys. Rev. B* **2011**, *83*, 245415/1–13. (c) Devid, E. J.; Martinho, P. N.; Kamalakar, M. V.; Šalitroš, I.; Prendergast, Ú.; Dayen, J.-F.; Meded, V.; Lemma, T.; González-Prieto, R.; Evers, F.; Keyes, T. E.; Ruben, M.; Doudin, B.; van der Molen, S. J. Spin Transition in Arrays of Gold Nanoparticles and Spin Crossover Molecules. *ACS Nano* **2015**, *9*, 4496–4507. (d) Pukenas, L.; Benn, F.; Lovell, E.; Santoro, A.; Kershaw Cook, L. J.; Halcrow, M. A.; Evans, S. D. Bead-Like Structures and Self-Assembled Monolayers from 2,6-Dipyrazolylpyridines and their Iron(II) Complexes. *J. Mater. Chem. C* **2015**, *3*, 7890−7896.

(15) (a) Nihei, M.; Han, L.; Oshio, H. Magnetic Bistability and Single-Crystal-to-Single-Crystal Transformation Induced by Guest Desorption. *J. Am. Chem. Soc.* **2007**, *129*, 5312–5313. (b) Nihei, M.; Takahashi, N.; Nishikawa, H.; Oshio, H. Spin-Crossover Behavior and Electrical Conduction Property on Iron(II) Complexes with Tetrathiafulvalene Moieties. *Dalton Trans.* **2011**, *40*, 2154–2156.

(16) (a) González-Prieto, R.; Fleury, B.; Schramm, F.; Zoppellaro, G.; Chandrasekar, R.; Fuhr, O.; Lebedkin, S.; Kappes, M.; Ruben, M. Tuning the Spin-Transition Properties of Pyrene-Decorated 2,6-Bispyrazolylpyridine Based Fe(II) Complexes. *Dalton Trans.* **2011**, *40*, 7564–7570. (b) Santoro, A.; Kershaw Cook, L. J.; Kulmaczewski, R.; Barrett, S. A.; Cespedes, O.; Halcrow, M. A. Iron(II) Complexes of Tridentate Indazolylpyridine Ligands: Enhanced Spin-Crossover Hysteresis, and Ligand-Based Fluorescence. *Inorg. Chem.* **2015**, *54*, 682–693.

(17) Abhervé, A.; Palacios-Corella, M.; Clemente-Juan, J. M.; Marx, R.; Neugebauer, P.; van Slageren, J.; Clemente-León, M.; Coronado, E. Bimetallic Mn^{III}–Fe^{II} Hybrid Complexes Formed by a Functionalized Mn^{III} Anderson Polyoxometalate Coordinated to Fe^{II}: Observation of a

Field-Induced Slow Relaxation of Magnetization in the M^{III} Centres and a Photoinduced Spin-Crossover in the Fe^{II} Centres. *J. Mater. Chem. C* **2015**, *3*, 7936−7945.

(18) (a) Hasegawa, Y.; Takahashi, K.; Kume, S.; Nishihara, H. Complete Solid State Photoisomerization of Bis(Dipyrazolylstyrylpyridine)Iron(II) to Change Magnetic Properties. *Chem. Commun.* **2011**, *47*, 6846–6848. (b) Takahashi, K.; Hasegawa, Y.; Sakamoto, R.; Nishikawa, M.; Kume, S.; Nishibori, E.; Nishihara, H. Solid-State Ligand-Driven Light-Induced Spin Change at Ambient Temperatures in Bis(dipyrazolylstyrylpyridine)iron(II) Complexes. *Inorg. Chem.* **2012**, *51*, 5188−5198.

(19) (a) Rajadurai, C.; Fuhr, O.; Kruk, R.; Ghafari, M.; Hahn, H.; Ruben, M. Above Room Temperature Spin Transition in a Metallo-Supramolecular Coordination Oligomer/Polymer. *Chem. Commun.* **2007**, 2636–2638. (b) Tovee, C. A.; Kilner, C. A.; Barrett, S. A.; Thomas, J. A.; Halcrow, M. A. A Back-to-Back Ligand with Dipyrazolylpyridine and Dipicolylamine Metal-Binding Domains. *Eur. J. Inorg. Chem.* **2010**, 1007–1012. (c) Botcha, A. K.; Basak, S.; Chandrasekar, R. Lithographically Organized 1D Nano-Tape Arrays Composed of Solution Processable Above Room Temperature Spin Cross-over Fe(II) Coordination Polymer. *RSC Adv.* **2014**, *4*, 34760–34763. (d) Kershaw Cook, L. J.; Fisher, J.; Harding, L. P.; Halcrow, M. A. An Iron(II) Spin-Crossover Metallacycle from a Back-to-Back Bis-[dipyrazolylpyridine]. *Dalton Trans.* **2015**, *44*, 9417–9425.

(20) Elhaïk, J.; Money, V. A.; Barrett, S. A.; Kilner, C. A.; Evans, I. R.; Halcrow, M. A. The Spin-States and Spin-Crossover Behaviour of Iron(II) Complexes of 2,6-Dipyrazol-1-ylpyrazine Derivatives. *Dalton Trans.* **2003**, 2053–2060.

(21) Mohammed, R.; Chastanet, G.; Tuna, F.; Malkin, T. L.; Barrett, S. A.; Kilner, C. A.; Létard, J.-F.; Halcrow, M. A. The Synthesis of New 2,6-Di(pyrazol-1-yl)pyrazine Derivatives, and the Spin State Behavior of their Iron(II) Complexes. *Eur. J. Inorg. Chem.* **2013**, 819–831.

(22) Bushuev, M. B.; Krivopalov, V. P.; Nikolaenkova, E. B.; Daletsky, V. A.; Berezovskii, G. A.; Sheludyakova, L. A.; Varnek, V. A. Spin Crossover Complex $[FeL^1_2](ClO_4)_2 \cdot H_2O$ (L^1 = 4-Methyl-2,6-bis(1H-pyrazol-1-yl)pyrimidine): Synthesis and Properties. *Polyhedron* **2012**, *43*, 81–88.

(23) (a) Gamez, P.; Reedijk, J. 1,3,5-Triazine-Based Synthons in Supramolecular Chemistry. *Eur. J. Inorg. Chem.* **2006**, 29–42. (b) Therrien, B. Coordination Chemistry of 2,4,6-Tri(pyridyl)-1,3,5-triazine Ligands. *J. Organomet. Chem.* **2011**, *696*, 637–651. (c) Safin, D. A.; Frost, J. M.; Murugesu, M. The Renaissance of 2,4,6-Tris(2-pyrimidyl)-1,3,5-triazine (TPymT) Coordination Chemistry. *Dalton Trans.* **2015**, *44*, 20287–20294.

(24) (a) Fu, L.-M.; Wen, X.-F.; Ai, X.-C.; Sun, Y.; Wu, Y.-S.; Zhang, J.-P.; Wang, Y. Efficient Two-Photon-Sensitized Luminescence of a Europium(III) Complex. *Angew. Chem. Int. Ed.* **2005**, *44*, 747–750. (b) Hao, R.; Li, M.; Wang, Y.; Zhang, J.; Ma, Y.; Fu, L.; Wen, X.; Wu, Y.; Ai, X.; Zhang, S.; Wei, Y. A Europium Complex with Excellent Two-Photon-Sensitized Luminescence Properties. *Adv. Funct. Mater.* **2007**, *17*, 3663–3669. (c) Stich, M. I. J.; Schaeferling, M.; Wolfbeis, O. S. Multicolor Fluorescent and Permeation-Selective Microbeads Enable Simultaneous Sensing of pH, Oxygen, and Temperature. *Adv. Mater.* **2009**, *21*, 2216–2220. (d) Law, G.-L.; Wong, K.-L.; Tam, H.-L.; Cheah, K.-W.; Wong, W.-T. White OLED with a Single-Component Europium Complex. *Inorg. Chem.* **2009**, *48*, 10492–10494. (e) Jiang, L.; Wu, J.; Wang, G.; Ye, Z.; Zhang, W.; Jin, D.; Yuan, J.; Piper, J. Development of a Visible-Light-

Sensitized Europium Complex for Time-Resolved Fluorometric Application. *Anal. Chem.* **2010**, *82*, 2529–2535. (f) Yu, J.; Sun, L.; Peng, H.; Stich, M. I. J. Luminescent Terbium and Europium Probes for Lifetime Based Sensing of Temperature Between 0 and 70 °C. *J. Mater. Chem.* **2010**, *20*, 6975–6981. (g) Xue, F.; Ma, Y.; Fu, L.; Hao, R.; Shao, G.; Tang, M.; Zhang, J.; Wang, Y. A Europium Complex with Enhanced Long-Wavelength Sensitized Luminescent Properties. *Phys. Chem. Chem. Phys.* **2010**, *12*, 3195–3202. (h) Shao, G.; Han, R.; Ma, Y.; Tang, M.; Xue, F.; Sha, Y.; Wang, Y. *Chem. Eur. J.* **2010**, *16*, 8647–8651. (i) Deng, W.; Jin, D.; Drozdowicz-Tomsia, K.; Yuan, J.; Wu, J.; Goldys, E. M. Ultrabright Eu–Doped Plasmonic Ag@SiO_2 Nanostructures: Time-gated Bioprobes with Single Particle Sensitivity and Negligible Background. *Adv. Mater.* **2011**, *23*, 4649–4654. (j) Lo, W.-S.; Zhang, J.; Wong, W.-T.; Law, G.-L. Highly Luminescent Sm^{III} Complexes with Intraligand Charge-Transfer Sensitization and the Effect of Solvent Polarity on Their Luminescent Properties. *Inorg. Chem.* **2015**, *54*, 3725–3727. (k) Tang, M.; Huang, Y.; Wang, Y.; Fu, L. An Ytterbium Complex with Unique Luminescence Properties: Detecting the Temperature Based on a Luminescence Spectrum without the Interference of Oxygen. *Dalton Trans.* **2015**, *44*, 7449–7457.

(25) (a) Gelling, A.; Orrell, K. G.; Osborne, A. G.; Sik, V. Synthesis and Solution Fluxionality of Rhenium(I) Carbonyl Complexes of 2,4,6-Tris(pyrazol-1-yl)-1,3,5-triazines (L), $[ReX(CO)_3L]$(X = Cl, Br or I). Characterization of $[\{ReX(CO)_3\}_2L]$ (X = Cl or Br). *J. Chem. Soc. Dalton Trans.* **1996**, 3371–3377. (b) Carrion, M. C.; Guerrero, A.; Jalón, F. A.; Manzano, B. R.; de la Hoz, A.; Claramunt, R. M.; Milata, V.; Elguero, J. Five Different Fluxional Processes in Polyfluorophenyl Palladium(II) Complexes with 2,4,6-Tris(3,5-dimethylpyrazol-1-yl)-1,3,5-triazine. The Driving Effect of the Solvent. *Inorg. Chem.* **2003**, *42*, 885–895. (c) Claramunt, R. M.; Cornago, P.; Cano, M.; Heras, J. V.; Gallego, M. L.; Pinilla, E.; Torres, M. R.

New Tris(pyrazolyl)triazine and Pyrazolylpyridine Gold(I) and Palladium(II) Derivatives Based on the 3,5-Bis(4-butoxyphenyl)pyrazole Group − Architectures with Different Types of Bonding Interactions. *Eur. J. Inorg. Chem.* **2003**, 2693–2704 and 3831 (correction). (d) Guerrero, A.; Jalón, F. A.; Manzano, B. R.; Rodríguez, A.; Claramunt, R. M.; Cornago, P.; Milata, V.; Elguero, J. Apparent Allyl Rotation in New Allylpalladium(II) Complexes with Pyrazolyl *N*-Donor Ligands. *Eur. J. Inorg. Chem.* **2004**, 549–556.

(26) (a) Zhou, H.-P.; Gan, X.-P.; Li, X.-L.; Liu, Z.-D.; Geng, W.-Q.; Zhou, F.-X.; Ke, W.-Z.; Wang, P.; Kong, L.; Hao, F.-Y.; Wu, J.-Y.; Tian, Y.-P. Anion-Induced Assembly of Five-Coordinated Mercury(II) Complexes and Density Functional Theory Calculations to Study Bond Dissociation Energies of Long Hg−N Bonds. *Cryst. Growth Des.* **2010**, *10*, 1767–1776. (b) Carranza, M. P.; Manzano, B. R.; Jalón, F. A.; Rodríguez, A. M.; Santos, L.; Moreno, M. First Examples of a Modulated Bridging μ_2-1:2κ*N*-Triazine in Double Helical Silver Compounds. Experimental and Theoretical Evidence. *Inorg. Chem.* **2010**, *49*, 3828–3835. (c) Yang, C.; Elbjeirami, O.; Gamage, C. S. P.; Dias, H. V. R.; Omary, M. A. Luminescence Enhancement and Tuning via Multiple Cooperative Supramolecular Interactions in an Ion-Paired Multinuclear Complex. *Chem. Commun.* **2011**, *47*, 7434–7436. (d) Carranza, M. P.; Manzano, B. R.; Jalón, F. A.; Rodríguez, A. M.; Santos, L.; Moreno, M. Experimental and Theoretical Evidence of Unsupported Ag–Ag Interactions in Complexes with Triazine-Based Ligands. Subtle Effects of the Symmetry of the Triazine Substituents. *New J. Chem.* **2013**, *37*, 3183–3194. (e) Wang, X.; Xing, Y. H.; Bai, F. Y.; Wang, X. Y.; Guan, Q. L.; Hou, Y. N.; Zhang, R.; Shi, Z. Synthesis, Structure, and Surface Photovoltage Properties of a Series of Novel d^7–d^{10} Metal Complexes with Pincer N-Heterocycle Ligands. *RSC Adv.* **2013**, *3*, 16021–16033. (f) Chen, C.; Sun, Q.; Ren, D.-X.; Zhang, R.; Bai, F.-Y.; Xing, Y.-H.; Shi, Z. Bromoperoxidase Mimic as Catalysts for

Oxidative Bromination—Synthesis, Structures and Properties of the Diversified Oxidation State of Vanadium(III, IV and V) Complexes with Pincer N-Heterocycle Ligands. *CrystEngComm* **2013**, *15*, 5561–5573. (g) Feng, X. D.; Zhang, R.; Wang, X. Y.; Zhang, X. X.; Wang, J. X. Xing, Y. H.; Sun, L. X. Mimicing Bromoperoxidase for Copper Complexes: Synthesis, Structures and Properties of Cu(II)–Triazine Pyrazolyl Complex. *Polyhedron* **2015**, *90*, 69–76.

(27) Wang, Z. N.; Wang, X.; Wei, S. Y.; Wang, J. X.; Bai, F. Y.; Xing, Y. H.; Sun, L. X. Triazine–Polycarboxylic Acid Complexes: Synthesis, Structure and Photocatalytic Activity. *New J. Chem.* **2015**, *39*, 4168–4177.

(28) Quiñonero, D.; Deyà, P. M.; Carranza, M. P.; Rodríguez, A. M.; Jalón, F. A.; Manzano, B. R. Experimental and Computational Study of the Interplay Between C–H/π and Anion–π Interactions. *Dalton Trans.* **2010**, *39*, 794–806.

(29) (a) Demeshko, S.; Dechert, S.; Meyer, F. Anion−π Interactions in a Carousel Copper(II)−Triazine Complex. *J. Am. Chem. Soc.* **2004**, *126*, 4508–4509. (b) Mooibroek, T. J.; Teat, S. J.; Massera, C.; Gamez, P.; Reedijk, J. Crystallographic and Theoretical Evidence of Acetonitrile−π Interactions with the Electron-Deficient 1,3,5-Triazine Ring. *Cryst. Growth Des.* **2006**, *6*, 1569–1574. (c) Casellas, H.; Massera, C.; Buda, F.; Gamez, P.; Reedijk, J. Crystallographic Evidence of Theoretically Novel Anion–π Interactions. *New J. Chem.* **2006**, *30*, 1561–1566. (d) Barrios, L. A.; Aromí, G.; Frontera, A.; Quinonero, D.; Deya, P. M.; Gamez, P.; Roubeau, O.; Shotton, E. J.; Teat, S. J. Coordination Complexes Exhibiting Anion···π Interactions: Synthesis, Structure, and Theoretical Studies. *Inorg. Chem.* **2008**, *47*, 5873–5881. (e) de Hoog, P.; Robertazzi, A.; Mutikainen, I.; Turpeinen, U.; Gamez, P.; Reedijk, J. An

Electron-Poor Host Receptor for Electron-Rich Guests Involving Anion–π and Lone-Pair–π Interactions. *Eur. J. Inorg. Chem.* **2009**, 2684–2690.

(30) (a) Medlycott, E. A.; Hanan, G. S.; Abedin, T. S. M.; Thompson, L. K. The Effect of Steric Hindrance on the Fe(II) Complexes of Triazine-Containing Ligands. *Polyhedron* **2008**, *27*, 493–501. (b) Hain, S. K.; Heinemann, F. W.; Gieb, K.; Müller, P.; Hörner, G.; Grohmann, A. On the Spin Behaviour of Iron(II)–Dipyridyltriazine Complexes and Their Performance as Thermal and Photonic Spin Switches. *Eur. J. Inorg. Chem.* **2010**, 221–232.

(31) (a) Young, M. C.; Liew, E.; Ashby, J.; McCoy, K. E.; Hooley, R. J. Spin State Modulation of Iron Spin Crossover Complexes via Hydrogen-Bonding Self-Assembly. *Chem. Commun.* **2013**, *49*, 6331–6333. (b) Sánchez-Sánchez, C.; Desplanches, C.; Clemente-Juan, J. M.; Clemente-León, M.; Coronado, E. Photomagnetic Properties of an Fe(II) Spin-Crossover Complex of 6-(3,5-Diamino-2,4,6-triazinyl)-2,2'-bipyridine and its Insertion into 2D and 3D Bimetallic Oxalate-Based Networks. *Dalton Trans.* **2017**, *46*, 2680–2689.

(32) See *eg* (a) Quesada, M.; de la Peña-O'Shea, V. A.; Aromí, G.; Geremia, S.; Massera, C.; Roubeau, O.; Gamez, P.; Reedijk, J. A Molecule-Based Nanoporous Material Showing Tuneable Spin-Crossover Behavior near Room Temperature. *Adv. Mater.* **2007**, *19*, 1397–1402. (b) Ross, T. M.; Moubaraki, B.; Neville, S. M.; Batten S. R.; Murray, K. S. Polymorphism and Spin Crossover in Mononuclear FeII Species Containing New Dipyridylamino-Substituted s-Triazine Ligands. *Dalton Trans.* **2012**, *41*, 1512–1523. (c) Wannarit, N.; Roubeau, O.; Youngme, S.; Gamez, P. Subtlety of the Spin-Crossover Phenomenon Observed with Dipyridylamino-Substituted Triazine Ligands. *Eur. J. Inorg. Chem.* **2013**, 730–737. (d) Scott, H. S.; Ross, T. M.; Chilton, N. F.; Gass, I. A.; Moubaraki, B.; Chastanet, G.; Paradis, N.; Lètard, J.-F.; Vignesh, K.

R.; Rajaraman, G.; Batten S. R.; Murray, K. S. Crown-Linked Dipyridylamino-Triazine Ligands and their Spin-Crossover Iron(II) Derivatives: Magnetism, Photomagnetism and Cooperativity. *Dalton Trans.* **2013**, *42*, 16494–16509. (e) Wannarit, N.; Nassirinia, N.; Amani, S.; Masciocchi, N.; Youngme, S.; Roubeau, O.; Teat, S. J.; Gamez, P. Drastic Effect of Lattice Propionitrile Molecules on the Spin-Transition Temperature of a 2,2′-Dipyridylamino/s-triazine-Based Iron(II) Complex. *Inorg. Chem.* **2014**, *53*, 9827−9836. (f) Scott, H. S.; Ross, T. M.; Phonsri, W.; Moubaraki, B.; Chastanet, G.; Lètard, J.-F.; Batten S. R.; Murray, K. S. Discrete Fe^{II} Spin-Crossover Complexes of 2,2′-Dipyridylamino-Substituted *s*-Triazine Ligands with Phenoxo, Cyanophenoxo and Dibenzylamino Functionalities. *Eur. J. Inorg. Chem.* **2015**, 763–777.

(33) Milata, V.; Claramunt, R. M.; Cabildo, P.; Santa María, M. D.; Cornago, P.; Infantes, L.; Cano, F. H.; Elguero, J. 2,4,6-Tris(azol-1-yl)-1,3,5-triazines: a New Class of Multidentate Ligands. *Heterocycles* **2001**, *55*, 905–924.

(34) Di Nicola, C.; Garau, F.; Marchetti, F.; Monari, M.; Pandolfo, L.; Pettinari, C.; Venzo, A. Synthesis, Characterization, Crystal Structure and Preliminary Reactivity Behaviour of New Heteropolytopic Ligands Based on the 1,3,5-Triazine Spacer and Pyrazolyl, Tris-Pyrazolylmethyl and Tris-Pyrazolylethoxy Bonding Fragments. *Dalton Trans.* **2011**, *40*, 4941–4953.

(35) Sheldrick, G. M. A Short History of *SHELX*. *Acta Cryst. Sect. A Found. Cryst.* **2008**, *64*, 112−122.

(36) Barbour, L. J. *X-Seed* – A Software Tool for Supramolecular Crystallography. *J. Supramol. Chem.* **2001**, *1*, 189−191.

(37) Dolomanov, O. V.; Bourhis, L. J.; Gildea, R. J.; Howard, J. A. K.; Puschmann, H. *OLEX2*: a Complete Structure Solution, Refinement and Analysis Program. *J. Appl. Cryst.* **2009**, *42*, 339–341.

(38) O'Connor, C. J. Magnetochemistry – Advances in Theory and Experimentation. *Prog. Inorg. Chem.* **1982**, *29*, 203–283.

(39) *SIGMAPLOT*, v. 8.02, SPSS Scientific Inc., Chicago IL, 2002.

(40) (a) Evans, D. F. The Determination of the Paramagnetic Susceptibility of Substances in Solution by Nuclear Magnetic Resonance. *J. Chem. Soc.* **1959**, 2003–2005. (b) Schubert, E. M. Utilizing the Evans Method with a Superconducting NMR Spectrometer in the Undergraduate Laboratory. *J. Chem. Educ.* **1992**, *69*, 62.

(41) García, B.; Ortega, J. C. Excess Viscosity η^E, Excess Volume V^E, and Excess Free Energy of Activation ΔG^{*E} at 283, 293, 303, 313, and 323 K for Mixtures of Acetonitrile and Alkyl Benzoates. *J. Chem. Eng. Data* **1988**, *33*, 200−204.

(42) *Spartan'16*, Wavefunction Inc., Irvine CA, USA, **2016**.

(43) Holland, J. M.; McAllister, J. A.; Kilner, C. A.; Thornton-Pett, M.; Bridgeman, A. J.; Halcrow, M. A. Stereochemical Effects on the Spin-State Transition Shown by Salts of $[FeL_2]^{2+}$ [L = 2,6-Di(pyrazol-1-yl)pyridine]. *J. Chem. Soc. Dalton Trans.* **2002**, 548–554.

(44) V_{Oh} is the volume of the octahedron defined by the FeN_6 coordination sphere.[53] Σ is a general measure of the deviation of a metal ion from an ideal octahedral geometry, while Θ more specifically indicates its distortion towards a trigonal prismatic structure. Σ and Θ are usually much larger in the high-spin than in the low-spin state; a perfectly octahedral complex gives $\Sigma =$

Θ = 0.[49,50] ϕ is the *trans*-N{azinyl}–Fe–N{azinyl} bond angle, while θ is the dihedral angle between the least squares planes of the two tridentate ligands. An undistorted D_{2d}-symmetric complex of this type will give ϕ = 180° and θ = 90°.[43] More detailed definitions of these parameters are in the cited references, and in the Supporting Information to this article.

(45) (a) Guerrero, A.; Jalon, F. A.; Manzano, B. R.; Claramunt, R. M.; Cabildo, P.; Infantes, L.; Cano, F. H.; Elguero, J. The Structure of Tris(3,5-Dimethylpyrazol-1-yl)-s-triazine and its Use as a Ligand in Coordination Chemistry. *Chem. Heterocycl. Comp.* **2003**, *39*, 1396–1403. (b) Ng, S. W. A Second Polymorph of 2,4,6-Tris-(3,5-di-methyl-1*H*-pyrazol-1-yl)-1,3,5-triazine. *Acta Cryst. Sect. E. Struct. Rep. Online* **2012**, *68*, o3201. Despite the title of reference (b), these two papers describe the same polymorph of L^3.

(46) (a) Manzur, J.; Acuna, C.; Vega, A.; Garcia, A. M. Copper(II) Assisted Hydrolysis of 2,4,6-Tris(pyrazol-1-yl)-1,3,5-triazine. Crystal and Molecular Structure of *catena*-$[CuL(H_2O)Cl]_n$ (L = 2,4-Dione-1,3,5-(1H)-triazin-1-amido). *Inorg. Chim. Acta* **2011**, *374*, 637–642. (b) Wang, J.-X.; Wang, C.; Wang, X.; Wang, X.-Y.; Xing, Y.-H.; Sun, Q. Experimental and Theoretical Investigations of Copper (I/II) Complexes with Triazine–Pyrazole Derivatives as Ligands and their In Situ C–N Bond Cleavage. *Spectrochim. Acta Part A: Mol. Biomol. Spectr.* **2015**, *142*, 55–61.

(47) A unit cell measurement established that the perchlorate salt $[Fe(L^2)_2][ClO_4]_2$ (cubic, $Ia\bar{3}d$, a = 18.6873(7) Å, V = 6525.9(4) Å^3, Z = 8 at 120 K) is isostructural with α-$[Fe(L^2)_2][BF_4]_2$.

(48) Kershaw Cook, L. J.; Kulmaczewski, R.; Cespedes, O.; Halcrow, M. A. Different Spin State Behaviors in Isostructural Solvates of a Molecular Iron(II) Complex. *Chem. Eur. J.* **2016**, *22*, 1789–1799.

(49) Guionneau, P.; Marchivie, M.; Bravic, G.; Létard, J.-F.; Chasseau, D. Structural Aspects of Spin Crossover. Example of the $[Fe^{II}L_n(NCS)_2]$ Complexes. *Top. Curr. Chem.* **2004**, *234*, 97−128.

(50) (a) McCusker, J. K.; Rheingold, A. L.; Hendrickson, D. N. Variable-Temperature Studies of Laser-Initiated $^5T_2 \rightarrow {}^1A_1$ Intersystem Crossing in Spin-Crossover Complexes: Empirical Correlations between Activation Parameters and Ligand Structure in a Series of Polypyridyl Ferrous Complexes. *Inorg. Chem.* **1996**, *35*, 2100−2112. (b) Marchivie, M.; Guionneau, P.; Létard, J.-F.; Chasseau, D. Photo-Induced Spin-Transition: the Role of the Iron(II) Environment Distortion. *Acta Cryst. Sect. B: Struct. Sci.* **2005**, *61*, 25–28.

(51) Vela, S.; Novoa, J. J.; Ribas-Arino, J. Insights into the Crystal-Packing Effects on the Spin Crossover of $[Fe^{II}(1\text{-bpp})_2]^{2+}$-Based Materials. *Phys. Chem. Chem. Phys.* **2014**, *16*, 27012–27024.

(52) Kershaw Cook, L. J.; Thorp-Greenwood, F. L.; Comyn, T. P.; Cespedes, O.; Chastanet, G.; Halcrow, M. A. Unexpected Spin-Crossover and a Low Pressure Phase Change in an Iron(II)/Dipyrazolylpyridine Complex Exhibiting a High-Spin Jahn-Teller Distortion. *Inorg. Chem.* **2015**, *54*, 6319−6330.

(53) (a) Haryono, M.; Heinemann, F. W.; Petukhov, K.; Gieb, K.; Müller, P.; Grohmann, A. Parallel Crystallization of a “Static” and a Spin-Crossover Polymorph of an Iron(II) Complex from the Same Solution. *Eur. J. Inorg. Chem.* **2009**, 2136–2143. (b) Takahashi, K.; Hasegawa,

Y.; Sakamoto, R.; Nishikawa, M.; Kume, S.; Nishibori, E.; Nishihara, H. Solid-State Ligand-Driven Light-Induced Spin Change at Ambient Temperatures in Bis(dipyrazolylstyrylpyridine)-iron(II) Complexes. *Inorg. Chem.* **2012**, *51*, 5188−5198.

(54) Boča, R. Zero-Field Splitting in Metal Complexes. *Coord. Chem. Rev.* **2004**, *248*, 757–815.

(55) (a) Elhaïk, J.; Evans, D. J.; Kilner, C. A.; Halcrow, M. A. A Structural, Magnetic and Mössbauer Spectroscopic Study of an Unusual Angular Jahn-Teller Distortion in a Series of High-Spin Iron(II) Complexes. *Dalton Trans.* **2005**, 1693–1700. (b) Elhaïk, J.; Kilner, C. A.; Halcrow, M. A. Structural Diversity in Iron(II) Complexes of 2,6-Di(pyrazol-1-yl)pyridine and 2,6-Di(3-methylpyrazol-1-yl)pyridine. *Dalton Trans.* **2006**, 823–830.

(56) (a) Houghton, B. J.; Deeth, R. J. Spin-State Energetics of Fe^{II} Complexes – The Continuing Voyage Through the Density Functional Minefield. *Eur. J. Inorg. Chem.* **2014**, 4573–4580. (b) Mortensen, S. R.; Kepp, K. P. Spin Propensities of Octahedral Complexes from Density Functional Theory. *J. Phys. Chem. A* **2015**, *119*, 4041−4050.

(57) Reiher, M.; Salomon, O.; Hess, B. A. Reparameterization of Hybrid Functionals Based on Energy Differences of States of Different Multiplicity. *Theor. Chem. Acc.* **2001**, *107*, 48–55.

(58) In the idealized D_{2d} symmetry of these complexes, the metal *d*-orbitals transform as: *e* (d_{xz} and d_{yz}); b_1 ($d_{x^2-y^2}$, which has π-symmetry with respect to the M–L bonds in the axis frame used); b_2 (d_{xy}, a M–L σ-symmetry orbital in this axis frame); and, a_1 (d_{z^2}). O_h symmetry labels are used in the text when the σ- and π-symmetry metal *d* orbitals are discussed collectively.

(59) The computed ligand bite angles (α) are within ±0.2° (low-spin molecules) or ±0.4° (high-spin) of the experimental values, where crystallographic data are available for comparison (Tables 2, S7 and S9). Hence, the differences between the computed bite angles of low-spin $[Fe(bpp)_2]^{2+}$ and $[Fe(bpt)_2]^{2+}$ and their derivatives ($1.0 \leq \Delta\alpha \leq 1.3°$) are large enough to be significant, and to explain the destabilization of the low-spin state in $[Fe(bpt)_2]^{2+}$.

(60) Gordon, A. J.; Ford, R. A. *The Chemists Companion: a Handbook of Practical Data, Techniques and References*, J. Wiley and Sons, New York, USA, 1972, pp. 108.

(61) (a) Bessel, C. A.; See, R. F.; Jameson, D. L.; Churchill, M. R.; Takeuchi, K. J. Structural Considerations of Terdentate Ligands: Crystal Structures of 2,2':6',''-Terpyridine and 2,6-Bis(pyrazol-1-yl)pyridine. *J. Chem. Soc. Dalton Trans.* **1992**, 3223–3228. (b) Echevarría, A.; Elguero, J.; Llamas-Saiz, A. L.; Foces-Foces, C.; Schultz, G.; Hargittai, I. Tris(pyrazol-1-yl)-s-triazine (TPT): X-ray Crystallographic, Computational, and Gas-Phase Electron Diffraction studies. *Struct. Chem.* **1994**, *5*, 255–264.

(62) Values of $\phi > 165°$ were treated as "almost linear" and defaulted to $\phi = 180°$ under the *SPARTAN'16* DFT protocol, so minimizations with fixed $165 \leq \phi \leq 180°$ could not be performed. They are expected to give $\Delta E(\text{dist}) \leq 0.3$ kcalmol^{-1} based on the results in Table 4, however.

(63) (a) Craig, D. C.; Goodwin, H. A.; Onggo, D. Steric Influences on the Ground State of Iron(II) in the Tris(3,3'-dimethyl-2,2'-bipyridine)Iron(II) Ion. *Aust. J. Chem.* **1988**, *41*, 1157–1169. (b) Onggo, D.; Goodwin, H. A. Steric Effects of the Spin State of Iron(II) in Complexes of Substituted Bipyridine Derivatives. *Aust. J. Chem.* **1991**, *44*, 1539–1551. (c) Arcis-Castíllo, Z.; Zheng, S.; Siegler, M. A.; Roubeau, O.; Bedoui, S.; Bonnet, S. Tuning the Transition

Temperature and Cooperativity of bapbpy-Based Mononuclear Spin-Crossover Compounds: Interplay between Molecular and Crystal Engineering. *Chem. Eur. J.* **2011**, *17*, 14826–14836.

(64) Phan, H.; Hrudka, J. J.; Igimbayeva, D.; Daku, L. M. L.; Shatruk, M. A Simple Approach for Predicting the Spin State of Homoleptic Fe(II) Tris-diimine Complexes. *J. Am. Chem. Soc.* **2017**, *139*, 6437−6447. This paper reports a correlation between the intra-ligand N…N-donor atom distance and metal ion spin state in $[FeL_3]^{2+}$ (L = a diimine chelate) derivatives, which is closely related to the ligand bite angles in those compounds.

(65) Swart, M.; Costas, M. (eds.), *Spin States in Biochemistry and Inorganic Chemistry: Influence on Structure and Reactivity*, John Wiley & Sons, Chichester, UK, 2016, p. 465.

FOR TABLE OF CONTENTS ONLY

Seven $[FeL_2]^{2+}$ complexes (L = a 2,4-di{pyrazol-1-yl}-1,3,5-triazine derivative) are all high-spin. This contrasts with related ligand types including 2,6-di{pyrazol-1-yl}pyridine, which are well known to afford spin-crossover iron(II) complexes. DF calculations imply this does not arise from the electronic properties of the triazinyl ligand donors. Rather, it predominantly reflects weaker σ-bonding to the pyrazolyl donors in $[FeL_2]^{2+}$, which can be attributed to a particularly narrow bite angle in the L ligand.